STScI | SPACE TELESCOPE SCIENCE INSTITUTE

Instrument Science Report WFC3 2026-03

Updated Time-Dependent Sensitivity Corrections for WFC3/UVIS

Aidan Pidgeon, Jennifer Mack, Varun Bajaj

September 14, 2026

Abstract

WFC3/UVIS image headers contain time-dependent inverse sensitivity values that may be used to properly convert detector count rates into physical units as the detector sensitivity changes over time. In-flight monitoring of CALSPEC standard stars is used to define these inverse sensitivity values for UVIS1 and UVIS2. With additional data from 2019 to 2026, we compute new linear best-fit solutions to the ratio of observed count rates to synthetic effective fluxes (obs/syn) derived using SEDs from CALSPEC. In addition, we incorporate revised encircled energy (EE) values from O'Connor et al. (2026), which introduce a scalar offset to the inverse sensitivity values for several filters. Errors in the linear fit coefficients are significantly improved with additional data, especially for UVIS2. We observe a wavelength dependence in the loss rates between 2011 and 2026, with UV filters losing sensitivity at roughly twice the rate of red filters (e.g. 0.2%/year in F225W, 0.1%/year in F814W). For a given dataset, the new solutions improve the agreement in the observed count rates (and the calculated effective fluxes) across the two detectors by 1-2% for some filters. Using the new linear fits to correct the observed photometry, we find the RMS scatter of the mean obs/syn flux ratio improves from 0.5% on each detector to 0.3% for UVIS1 and 0.2% for UVIS2. These updates may be important for high-precision photometry—such as stellar SED modeling—where the target spans both detectors, or for observations of a target acquired over several years. An updated photometry reference file will be delivered later in 2026 for reprocessing all archival UVIS images. Until then, we provide a workflow for manually correcting the observed count rates in calibrated images.

Copyright© 2026 The Association of Universities for Research in Astronomy, Inc. All Rights Reserved.

1 Introduction

The Wide Field Camera 3 (WFC3) UVIS channel consists of two charge-coupled device (CCD) detectors (chips): UVIS1 and UVIS2. Each has a unique time-dependent sensitivity (TDS) solution to provide accurate photometric calibration across the lifetime of the instrument. Over time, a variety of methods have been used to calibrate the UVIS channel.

The first in-flight calibration was based on observations of two CALSPEC [1] white dwarf standards, GD153 and GRW+70 5824 (hereafter GRW70), observed in the Amplifier (Amp) A corner subarray, close to the readout (see Kalirai et al. 2009). A chip-dependent photometric calibration was first described by Deustua et al. (2016) to account for differences in the wavelength-dependent response of the two CCDs. These results were used to compute an inverse-sensitivity value for UVIS1 and UVIS2 in each filter, based on observations of the three HST primary white dwarf standards (GD153, G191B2B, and GD71) in the Amp A and Amp C corner subarrays.

Additional monitoring data showed that the sensitivity of each detector was changing, with the observed count rates declining as much as $\sim 0.2\%$ per year, depending on the filter (see Gosmeyer et al. 2014, Shanahan et al. 2017, and Khandrika et al. 2018). By 2019, losses had reached nearly 2% in the popular F606W filter, and Calamida et al. (2021) computed new time-dependent inverse sensitivity values using photometery of the same three primary white dwarfs, plus the secondary white dwarf standard (GRW70) and the G-type standard P330E for red filters (pivot wavelengths $> 5{,}880$ Å). These values were incorporated into the image photometry table (IMPHTTAB) reference file used by `calwf3` to populate photometric keywords in the header of each calibrated FLT or FLC image.

In this report, we provide updated TDS corrections derived from linear fits to the observed-to-synthetic photometry of the same five CALSPEC standards used by Calamida et al. and the same version of the observed SEDs, i.e. (*_stiswfcnic_002.fits*). The new solutions therefore provide a relative "delta" correction to the values in the IMPHTTAB, *51c1638pi_imp.fits*, in which the intercept of the linear fit is used to scale the inverse sensitivity values at the WFC3 reference epoch in June 2009 (MJD=55008). While a more recent set of SEDs are available in CALSPEC, these have negligible flux differences ($< 0.1\%$ in all WFC3 imaging filters) with respect to the SEDs used for this work.

In Section 2, we describe the data sample selected for analysis and the methods used for both aperture and synthetic photometry. In Section 3, we define the TDS models for visible- and for UV- filters, while in Section 4, we compare the TDS loss rates with wavelength, and we quantify the scalar offsets required to the reference-epoch inverse sensitivity values. In Section 5, we test the new TDS models by comparing relative photometry of the globular cluster ω Cen over 16 years in F606W, and we show the improvement in the UVIS2 flux at the current epoch for the white dwarf GRW70 in F555W. In Sections 6 and 7, we summarize the conclusions of this work and provide recommendations for users.

Updated inverse sensitivity values and photometric zeropoints will be delivered alongside the new EE tables and an updated IMPHTTAB reference file, to be used for reprocessing all UVIS images in the Mikulski Archive for Space Telescopes (MAST) by late-2026. In the

[1] `https://www.stsci.edu/hst/instrumentation/reference-data-for-calibration-and-tools/astronomical-catalogs/calspec`

interim, we provide a worked example in the appendix of this report for correcting UVIS photometry using keyword values populated in the image headers and updated tables with the new inverse senstivity and slope values for each filter on UVIS1 and UVIS2.

2 Photometric Data

Each HST cycle, the WFC3 team designs calibration programs to monitor several CALSPEC spectrophotometric standards, including the three HST primary white dwarfs (WDs) GD153, GD71, G191B2B and the secondary white dwarf GRW+70 5824 (GRW70). In addition to white dwarfs, the G-type star P330E and the A-type star TYC 4212-455-1 (referred to as 1757132 in CALSPEC) are observed to measure any color terms. Observations of these stars began at WFC3's installation in 2009, with the exception of TYC 4212-455-1, which was added in 2021. These standards are observed using the 512×512-pixel UVIS corner subarrays, enabling independent measurements of sensitivity changes for each UVIS detector, while minimizing flux losses due to degradation of charge transfer efficiency (CTE).

Exposures are designed to achieve a minimum signal-to-noise ratio (SNR) of ∼100 and an average SNR of ∼500. This report uses data from 30 HST CAL programs from 2009 to 2026, including IDs: 11426, 11450, 11903, 11907, 12333, 12698, 13088, 13089, 13574, 13575, 13711, 14018, 14021, 14382, 14384, 14815, 14883, 14992, 15113, 15398, 15399, 15582, 15583, 16030, 16415, 16579, 17015, 17361, 17681, and 17960. Links to individual programs are provided on the WFC3 Calibration Plan webpage[2] for each HST observation cycle.

Observations of each star were downloaded in the form of calibrated, CTE-corrected exposures (FLCs) from the MAST. The images were then analyzed with a Python script—described in section 2.1—based on the `Photutils`[3] package. Drizzled data products (DRCs) were not used, as these typically require custom reprocessing to optimize the cosmic-ray rejection and image stacking, which is beyond the scope of this work.

With six years of additional monitoring since the analysis by Calamida et al. (2021), we selected only observations in the Amp A (UVIS1) and Amp C (UVIS2) corner subarrays in our analysis. Observations in the Amp B (UVIS1) and Amp D (UVIS2) corner subarrays are more rarely taken and require normalization to the Amp A and Amp C count rates, respectively, which could potentially introduce systematic errors. Flat field uncertainties in the corner subarrays were estimated by Khandrika et al. (2018) by comparing the observed count rates of the three primary CALSPEC white dwarfs. For the F606W filter, for example, offsets of -1.4% between Amps A and B and -1.1% between Amps C and D were reported.

We also exclude spatial scan observations; though these provide excellent photometric repeatability, they cannot be normalized to synthetic photometry in the same way as staring mode data. Calamida et al. include spatial scan photometry, e.g. GRW70 and GD153 count rates were scaled to the mean count rate for staring mode photometry over the same ~ 3 year time interval (from 2016.8 to 2019.8). Because scanned photometry was not available for the first ~ 7 years, we exclude it to avoid introducing systematic errors in the combined fit.

[2]https://www.stsci.edu/hst/instrumentation/wfc3/calibration-plan
[3]https://photutils.readthedocs.io/en/stable/

2.1 Aperture Photometry

We create a custom photometry pipeline to obtain the photometric measurements used for our analysis, which performs the following steps:

Source Detection: The pipeline uses the `find_sources` function from `Photutils` on each FLC image, set to a detection threshold of 100 contiguous pixels that each contain $\geq$ 30 e^-. If no source is detected, the threshold is lowered to 75 pixels containing 15 e^- each. Images with no detected source using the lowered threshold are rejected; this occurs for $< 1\%$ of images. If more than one source is found in an image, the target coordinates from the image header (keywords `RA_TARG` and `DEC_TARG`) are compared to the coordinates of each detected source after accounting for proper motions, which are obtained from the SIMBAD database, and the closest match is kept.

Distortion and Unit Correction: Due to the tilt of the detector in the focal plane, UVIS pixels subtend unequal areas of the sky. However, in the flat-fielding step of the calibration pipeline the area of each pixel (as well as relative sensitivity of the pixel) is divided out, thus "flattening" the surface brightness (but no longer representing flux). Images are multiplied by the UVIS Pixel Area Map (PAM, Kalirai et al. 2010) to convert the images back to flux space; then divided by exposure time to convert to units of e^-/s.

Background Subtraction: Sky background is measured as the 3σ clipped mean in a 9-pixel wide annulus with an inner radius of 156 pixels, and is subtracted from the image. This is the same annulus used by Calamida et al. for UVIS photometric calibration.

Aperture Photometry: Source flux is measured within 10-pixel radius apertures. Uncertainties are calculated with the method used by `IRAF/DAOPHOT` (Stetson, 1987).

PHTRATIO Correction: The `FLUXCORR` step of the `calwf3` pipeline multiplies UVIS2 science arrays by the inverse sensitivity ratio, or `PHTRATIO`, equal to `PHTFLAM2/PHTFLAM1`. Rather than rerunning `calwf3` with `FLUXCORR` set to `OMIT`, we can back out this correction by dividing photometry for UVIS2 targets by the time-dependent `PHTRATIO` value populated in the science image header. This allows us to work with the original count rates measured on each detector.

2.2 Synthetic Photometry

Synthetic count rates were calculated using the `Synphot`[4] and `STSynphot`[5] Python packages. A synthetic source was created for each standard star using the same CALSPEC SEDs (*_stiswfcnic_002.fits*) used by Calamida et al. (2021) for UVIS photometric calibration. These synthetic spectra were combined with bandpasses for each observing mode, i.e. each combination of filter and UVIS detector, to generate a synthetic observation. We used these synthetic observations to predict the flux of each source (in electrons per second) in a 10-pixel aperture at the reference epoch of MJD = 55008 (June 26, 2009), which corresponds to the beginning of WFC3's on-orbit operation.

[4]https://synphot.readthedocs.io/en/latest/

[5]https://stsynphot.readthedocs.io/en/latest/

As `STSynphot` does not yet account for the updated EE corrections at 10 pixels (see Table 7 from O'Connor et al. 2026), the synthetic count rates were corrected to use these updated EE values. The new EE tables are based on deep observations of stars with high enough SNR at large radii to reliably measure the EE fraction between 0.″4 (10 pixels) and 6″, which is used for computing the photometric zeropoints. Notable changes to the EE at 10 pixels, EE(10), are listed here:

- The new UVIS2 EE(10) value is 0.5% larger than the prior EE(10) value for F775W, F814W, and F845M.
- The EE(10) for F850LP is nearly 2% smaller than Calamida et al., who adopted the F814W EE values for this filter.
- For UV filters (F218W, F225W, F275W), the EE(10) was under-estimated due to reliance on an optical model of the PSF (Hartig, 2009) that over-predicted the fraction of light enclosed at large radii.

The ratio of an observed photometric measurement to a synthetic equivalent (obs/syn) can then be treated as a measure of change in sensitivity since that reference epoch. However, the values of the synthetic photometry are themselves based upon the analysis of Calamida et al., since the synthetic bandpasses used by `STSynphot` were derived using the weighted average of the observed photometry from that analysis. The updated inverse sensitivity values presented in this report are calculated relative to the reference-epoch inverse sensitivity values from Calamida et al. which are contained in the IMPHTTAB (*51c1638pi_imp.fits*) delivered in late-2020, where the intercept of the linear fit is used to scale the inverse sensitivity value at the WFC3 reference epoch of MJD=55008.

3 TDS Models

A methodology similar to Calamida et al. (2021) was used for calculating TDS models from the obs/syn data. For visible-wavelength filters with pivot wavelengths (λ_p) > 3000 Å, we used a single linear fit to the data (see section 3.1). For UV-filters, the observed count rates increase for the first $\sim$ 2 years on-orbit, followed by a steady decline. For this reason, UV data were fit to a piecewise function with two line-segments (see section 3.2).

To mitigate the possible impact of errors in the CALSPEC SEDs, we computed separate linear fits for each star. We then computed a weighted mean slope for each detector and filter including only stars with sufficient data for a reliable solution (see section 3.1). This slope, with its 3σ error, was then used as a bounds for the combined fit. This differs from the approach by Calamida et al. who computed least-square linear fits to the combined set of obs/syn measurements from all stars.

3.1 Visible-Wavelength Filters

Before fitting the obs/syn data, we clipped a small number of outliers with obs/syn ratios differing by more than 10% from unity. Next, we calculated an initial fit using all remaining

data for that observing mode. We then normalized the data using the initial fit results for each star, and we clipped outliers differing by more than 3σ from the mean of the residuals. These points were then removed from the sample before further analysis.

Observed-to-synthetic flux ratios for each star can be systematically offset due to uncertainties in the absolute flux of the CALSPEC SEDs. Fitting to the entire data sample at once (all the targets in a given filter) can therefore lead to spurious results, especially when different targets have been observed at irregularly-spaced intervals. To mitigate the impact of offsets in the obs/syn ratio, we bound the final linear fit using slope values derived from fits to the obs/syn ratio of individual stars. For each observing mode, we fit data from targets that met two criteria:

- The target was observed in that specific mode during four or more HST visits.
- Those visits span a minimum baseline of 6 years ($> 1/3$ of WFC3's on-orbit lifetime).

The slope terms for each of the single-target fits for a given observing mode were combined in an inverse variance-weighted mean. A range of 3σ about these weighted-mean slopes was then used to bound the slope of the final fit to the ensemble of the data. For a few filters, none of the stars had sufficient data to meet the criteria for fitting (see entries marked with an asterisk in Table 1 and Table 2). In those cases, we used the slope from a wide-band filter with a bandpass that overlaps the narrow-band filter and a range of plus or minus 3σ to bound the slope values.

This method ensures that the intercept term in the final linear fit, used to update the inverse sensitivity at the reference epoch, can be based upon all available data, while the slope terms avoid undue influence from unevenly-spaced observations. To match the methodology of Calamida et al., we also include P330E in fits for all filters with $\lambda_p \geq 5880$ Å.

As discussed in section 2.2, normalizing the observed photometry by its synthetic photometry introduces a dependence on the previous solution. The updated inverse sensitivity values are therefore relative to that solution and calculated by dividing the reference-epoch inverse sensitivity values from the 2020 IMPHTTAB by the intercept of the final linear fit.

Obs/syn photometry and model fits for the F606W filter are presented in Figure 1. Model coefficients (slopes and intercepts) and updated inverse sensitivity values are provided in Table 1 and Table 2 of Appendix A. A worked example for correcting UVIS photometry using the new models is provided in Appendix B for the F475W filter, which has a significantly steeper UVIS2 slope than reported by Calamida et al. (2021). Plots for other frequently used filters are provided in Appendix C for wide-band (W) filters (F336W, F390W, F438W, F475W, F555W, F625W, F775W, F814W), and for one representative medium-band (M) filter F410M, one narrow-band (N) filter F657N, and one long-pass (LP) filter F850LP.

Filters with predicted fluxes that differ from the IMPHTTAB prediction by more than 0.5% (W, M), 1.0% (LP, X), or 1.5% (N) at any time between 2009 and 2026 are highlighted with bold-face font in the tables. For UVIS1, this is limited to a few medium, narrow, and long-pass filters. **For UVIS2, significant improvements in the slopes and intercept estimates are found with the longer time baseline and the new EE estimates**. Improving the slope for a single detector improves the time-evolved PHTRATIO values at the current epoch, i.e. the count rates on UVIS1 and UVIS2 on a given FLC image observed at the present day will now better agree, in addition to more accurately estimating the flux.

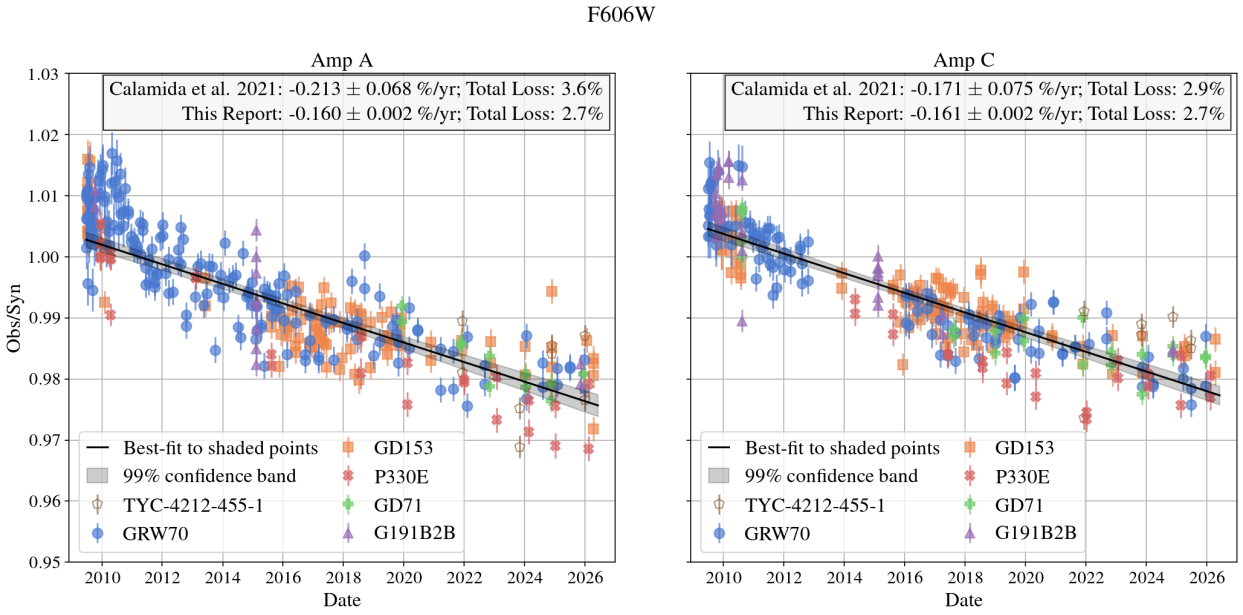

Figure 1: Obs/syn photometry for the F606W filter and the best-fit line for UVIS1 (left) and UVIS2 (right). Targets that do not contribute to the final linear fit are drawn with hollow markers. The model slope and the total loss (percent decrease in observed count rate) over the $\sim$ 17 year instrument lifetime are reported in the legend. The slope and the total loss predicted from Calamida et al. (2021) are provided for comparison. The shaded area about the fit line represents the 99% confidence band for the fit.

Fluxes for a large number of narrow-band filters differ by more than 1.5% from the IMPHTTAB prediction. For filters lacking enough measurements to compute a reliable slope, Calamida et al. substituted the slopes of filters with similar pivot wavelengths. Additional monitoring data have allowed us to fit models to all narrow filters that previously lacked sufficient data to do so. However, unlike the wide and medium filters above, our fits for most narrow filters are still based on few datasets and have larger uncertainties.

3.2 UV Filters

Photometry in WFC3 UV filters ($\lambda_p < 3000$ Å) shows that sensitivity increases for the first $\sim$ 2 years of the instrument's lifetime before declining thereafter (Shanahan et al., 2017; Khandrika et al., 2018). This behavior in the UV has been observed for multiple HST detectors, e.g. by Carlberg & Monroe (2017). Similarly to (Calamida et al., 2021), we fit two line segments for these filters; one for the first two years of WFC3 observations (MJD 55008 to 55737) and a second for observations taken from MJD 55738 to the present. Outlier clipping was performed separately for each segment, using the same method as the visible wavelength filters: normalizing each segment with independent initial slopes, then performing a 3σ clip and removing the clipped points from further analysis.

Our method differs from that of Calamida et al. in fitting these segments as a piecewise function—rather than independently—to ensure continuity at the break point. This is cal-

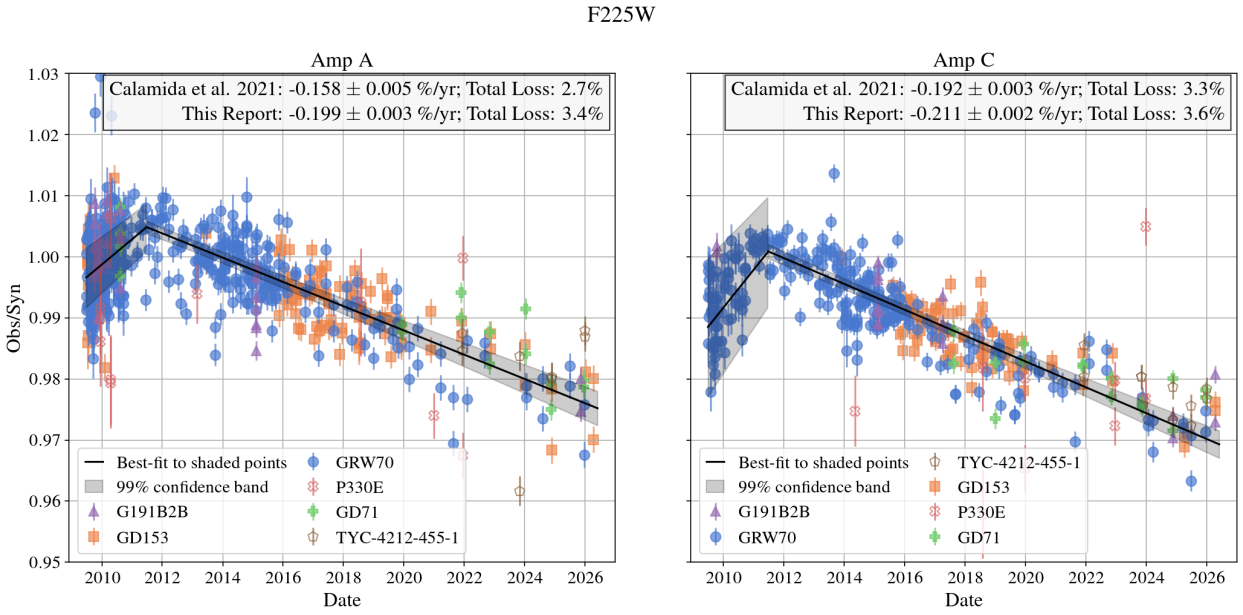

Figure 2: The obs/syn photometry and best-fit lines for the F225W filter. Targets that do not contribute to the final linear fit are drawn with hollow markers. The slope after the turnover at MJD $\geq$ 55738 and the total loss in the observed countrate are reported in the legend. The slopes and losses predicted by Calamida et al. (2021) are provided for comparison. Confidence bands are similar to those in Figure 1, but are calculated separately for each segment.

culated with a fit to three free parameters: the reference-epoch intercept and the slope of each segment. For each segment, we still fit models to individual targets and then took an inverse variance-weighted mean of the slope terms, $\pm 3\sigma$, to bound the final model's slopes. For the second line segment, the selection criteria for targets to fit individually were kept the same as for the non-UV filters; targets must have been observed in least four visits over a span of six years. For the first segment, we kept the requirement for number of visits, but reduced the required time-span to six months. For modes where no individual targets met these criteria, we used the slope of an overlapping wide-band filter $\pm 2\%$/yr to bound the final model.

The obs/syn photometry and models for the F225W filter are shown in Figure 2. **Model coefficients for the UV filters are listed in Table 3 and Table 4 of Appendix A**. A few outliers are evident in the plots, with 1-2% deviations from the model even after sigma clipping the detrended data, as described in section 3. We visually examined these images and confirmed the presence of either faint cosmic rays or bad pixels within the 10 pixel radius aperture. Since there are relatively few of these, compared to the total number of observations, we choose to include them rather than adjusting the sigma clipping to avoid any possible over-rejection in the data sample.

4 Analysis

4.1 Wavelength- and Chip-Dependence

With a longer temporal baseline of observations, the uncertainties in the model fits are reduced compared to prior analyses. As a result, the TDS loss rates now show a clear wavelength dependence, with F225W losing sensitivity at nearly twice the rate of F814W. The slopes for both UVIS detectors are now similar to one another, as shown in Figure 3, with UVIS1 losing sensitivity slightly faster than UVIS2 for filters with a pivot wavelength between 3900-7500 Å. Differences in slope between detectors are less than 0.05% per year for all wide and medium filters, with F621M and F775W showing the largest differences.

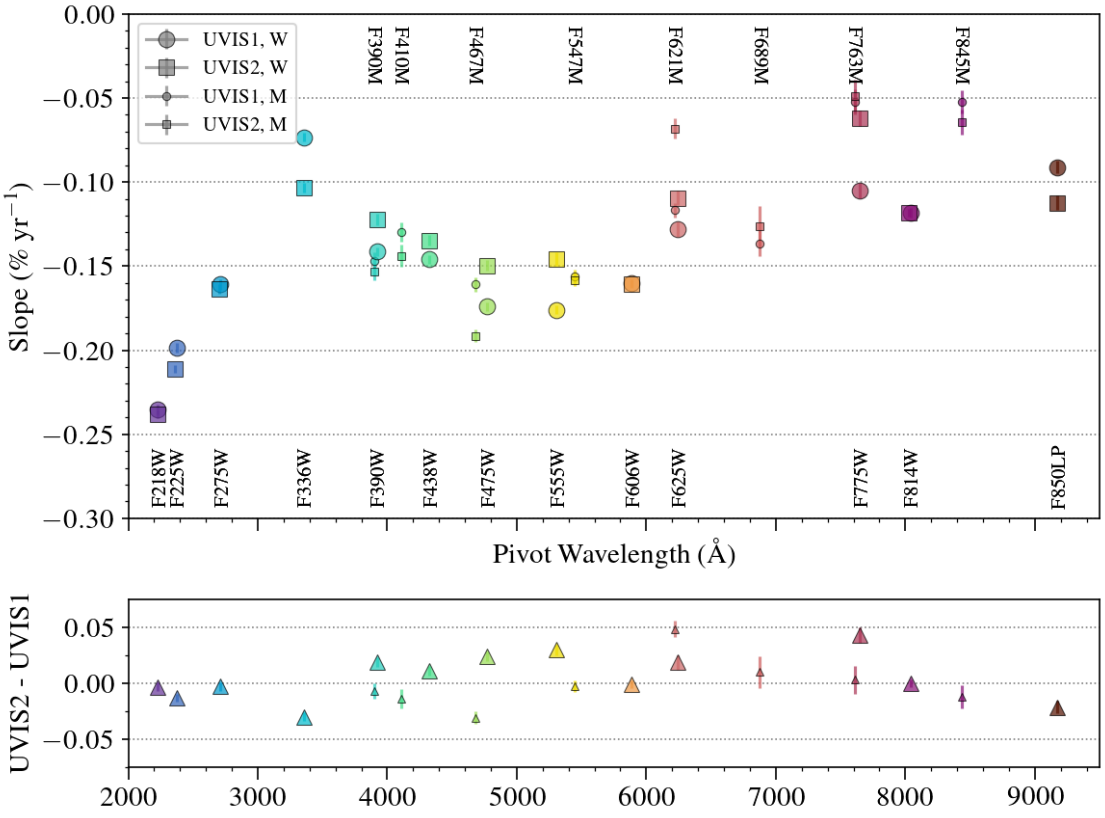

Figure 3: Slopes for wide and medium filters (plus F850LP), as a function of filter pivot wavelength. Slopes for F218W, F225W, and F275W are for the second line segment after 25 Jun 2011 (MJD $\geq$ 55737). Differences in slopes between the two UVIS chips are shown in the lower panel.

F336W is the notable exception to the wavelength-dependent difference in slopes between the chips, with its UVIS1 slope shallower than its UVIS2 slope. On examination, the UVIS1 obs/syn data, shown in Figure 9 of Appendix C, is not well-modeled by a single line segment and could be fit with 2 segments, as for the UV filters. For consistency with prior work, we use a single line segment to model this filter, but the changing rate of sensitivity decline suggests

that using a different approach to model the TDS may be beneficial in future work, e.g. using multiple line segments—similar to the UV filters in section 3.2; or to STIS, (Carlberg & Monroe, 2017))—or a rolling average—similar to ACS/SBC, (Avila et al., 2019).

Figure 4 is similar to Figure 3, but plots the intercept offset to the model fit to the obs/syn ratio as a function of pivot wavelength for all wide- and medium- filters. This offset is equivalent to the percentage change in the reference-epoch inverse sensitivity values compared to the IMPHTTAB values derived by Calamida et al.. A difference in intercepts across chips, therefore, is representative of a change to the inverse sensitivity ratio (`PHTRATIO`) at the reference epoch.

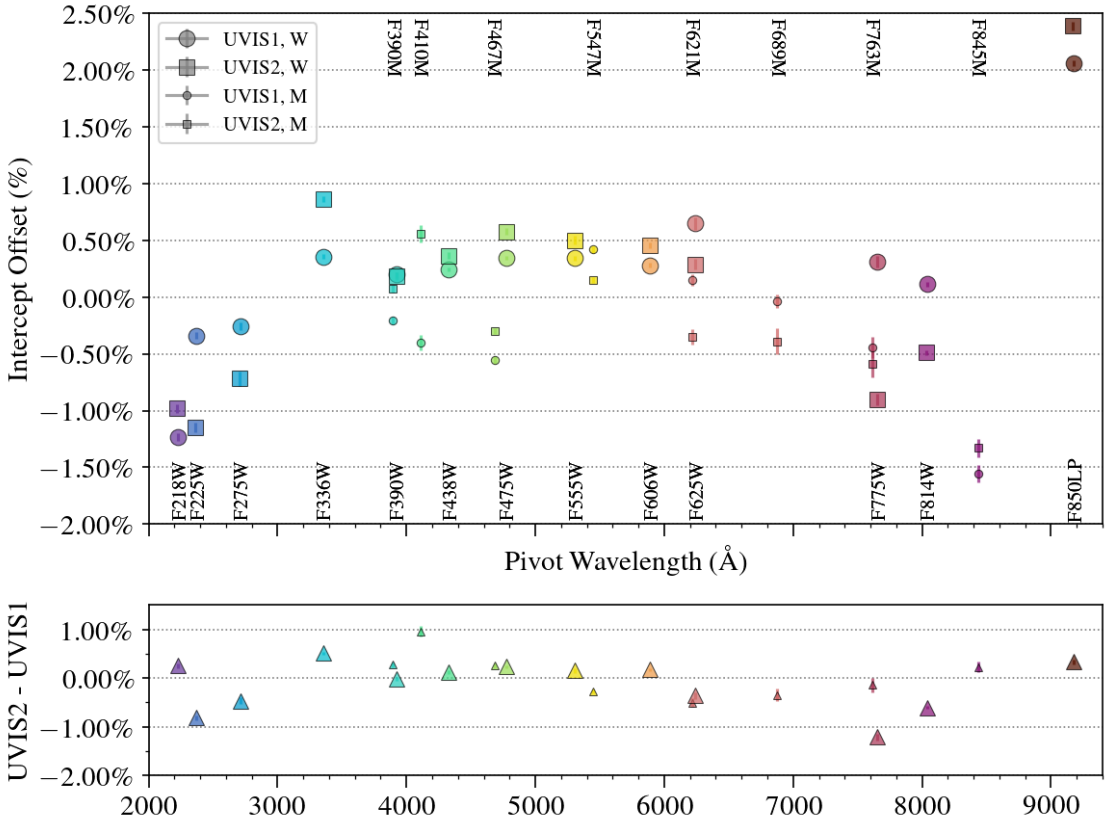

Figure 4: Intercept offsets (from unity) for wide and medium filters, plus F850LP, as a function of filter pivot wavelength. Intercepts for F218W, F225W, and F275W are for the first line segment (MJD $\leq$ 55737). Differences in the intercept offset (UVIS2-UVIS1) are shown in the lower plot and correspond to changes in the inverse sensitivity ratio at the reference epoch, PHTRATIO$_{ref}$, with the F775W value differing by more than 1% compared to the values in the IMPHTTAB.

For wide filters, F775W has the largest slope difference between the two chips ($\approx 0.5\%$) and the greatest change in the intercept between chips, with (UVIS2-UVIS1) = -1.2%. However, for F775W the intercept is positive on UVIS1, but the slope is steeper than predicted, whereas on UVIS2, the intercept is negative but the slope is shallower (see Figure 16).

For many filters, including F625W and F775W, early monitoring was limited to UVIS1, with UVIS2 added around 2014 (see Figure 15 and Figure 16 of Appendix C), resulting in larger errors in the predicted slopes. For example, for F625W the UVIS2 slope was too steep (-0.187%/yr vs -0.109%/yr), over-predicting the cumulative loss in 2026 by $\approx 1.4\%$, based on slopes alone. Using the combined fit with the intercept (+0.29%), the difference in the ratio for UVIS2 in 2026 is: obs/syn$_{new}$ = 1.0029 − 0.00109%/yr × 17 yr = 0.984, obs/syn$_{old}$ = 1.0 − 0.00187%/yr × 17 yr = 0.968, and the difference (new-old) is **0.016.** While the UVIS1 slopes are similar to the predicted values to within the uncertainties, the intercept is larger (+0.65%) so that the total flux difference in 2026 is less than the prediction based on slopes alone: obs/syn$_{new}$ = 1.0065 − 0.00128%/yr × 17 yr = 0.985, obs/syn$_{old}$ = 1.0000 − 0.00155%/yr × 17 yr = 0.974, and the difference (new-old) is **0.011**.

These differences show that fitting line segments to the observed photometry for each CCD is sensitive to any differences in cadence of the observations. For example, UVIS2 monitoring for several stars did not begin until mid-2014, and therefore errors in the IMPHTTAB slopes and intercepts, derived using data from 2014 to 2019, were larger than for UVIS1. With the new analysis, we include ~ 7 years of additional observations, and statistical errors are now more similar for the same filter on different CCDs.

4.2 Obs/Syn Residuals

To check the effectiveness of the new linear fits, we correct the obs/syn photometry by the new slope and intercept values and then compute the inverse-variance weighted mean of the corrected obs/syn for each target. These values are plotted as a function of pivot wavelength in Figure 5 for wide and medium filters, plus the long-pass filter F850LP. The root mean square error (RMSE) about unity for the W and M filters is 0.31% on UVIS1, and 0.22% on UVIS2. This represents a significant improvement compared to the previous RMSE of 0.5% for each CCD in Figures 14 and 15 of Calamida et al. (2021). Values for narrow-band filters are shown in Figure 6. The RMSE for these filters is greater than for the wider filters, but is still $< 1\%$ on both chips, at 0.55% for UVIS1 and 0.81% for UVIS2.

In Figure 5, we also see that the G-type standard P330E and the A-type TYC-4212-455-1 have obs/syn values < 1.0 for most filters, with a mean across all filters that is ~ 0.5 % lower than the average of CALSPEC white dwarfs. On the other hand, the white dwarfs cluster near unity in the weighted average, because the bulk of the UVIS photometric monitoring observations are based on these standards. The small baseline of observations for TYC-4212-455-1 make it difficult to draw a conclusion based on its offset, but the more robust data set for P330E points to a real systematic. Notably, the photometric calibration of the ACS/WFC by Bohlin et al. (2020b) shows a similar offset for P330E in several filters, pointing to a detector-independent effect. One possible source could be small errors in the CALSPEC *_stiswfcnic_002.fits* SEDs for the non-white dwarf targets, used in this work for consistency with Calamida et al.

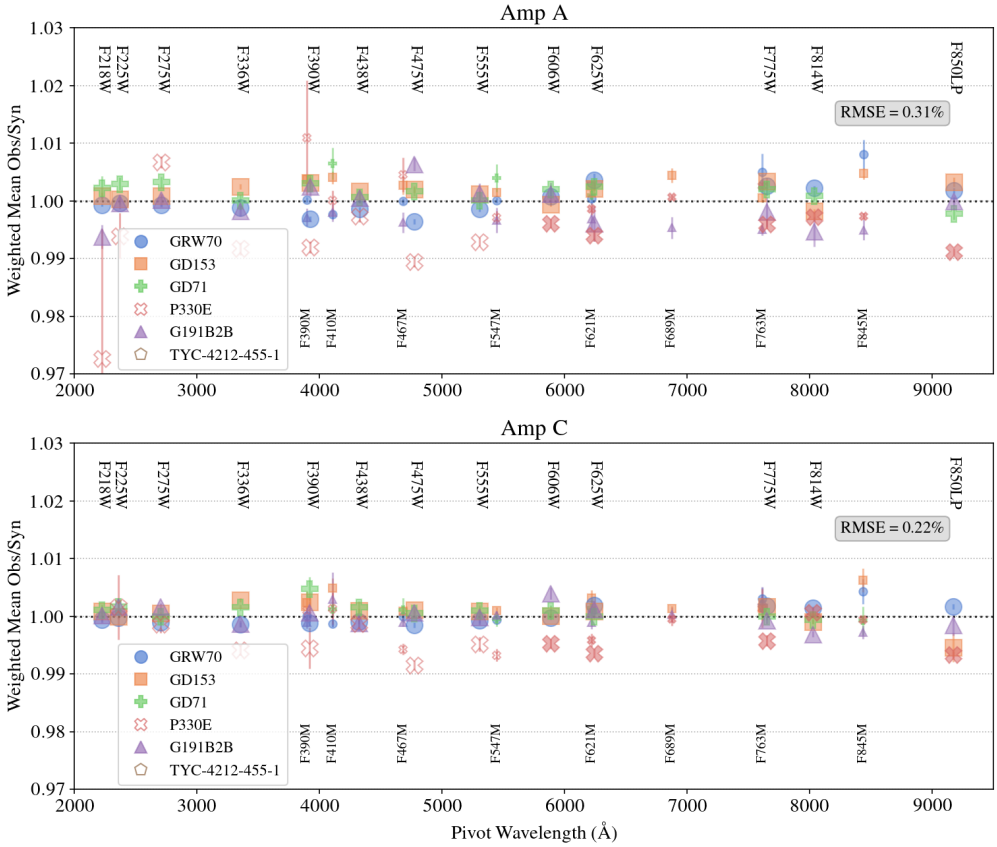

Figure 5: Weighted mean obs/syn flux ratio for amp A (top) and amp C (bottom) by target at the 2009 reference epoch (MJD=55008) as a function of filter pivot wavelength, for wide and medium filters plus F850LP. (Open symbols show targets excluded from the combined linear fit for that filter). Correcting the observed count rates using the new TDS models reduces the RMS error in the obs/syn ratio from 0.5% in (Calamida et al., 2021) to 0.3% on UVIS1 and 0.2% on UVIS2.

5 Validating the New TDS Models

5.1 Globular Cluster: ω Centauri

We validated our solutions using observations of the core of the ω Cen globular cluster collected with the F606W filter over a 16+ year baseline, as part of the WFC3/UVIS Distortion Monitor. Observations span a range of orientation values, so the position of each star was cross-matched across all images into a master catalog.

We performed aperture photometry with a 5-pixel radius and corrected to 10 pixels using spatially-variable aperture correction maps from Huynh et al. (2025) and focus values computed via HST1PASS, as described in the aforementioned report. To minimize effects due to photometric precision errors, we use only unsaturated stars with fluxes of $\geq$ 2000 electrons within the aperture. To mitigate sampling bias, we simultaneously solve for stellar magnitudes and image-specific offsets using a robust sparse least-squares optimization. By

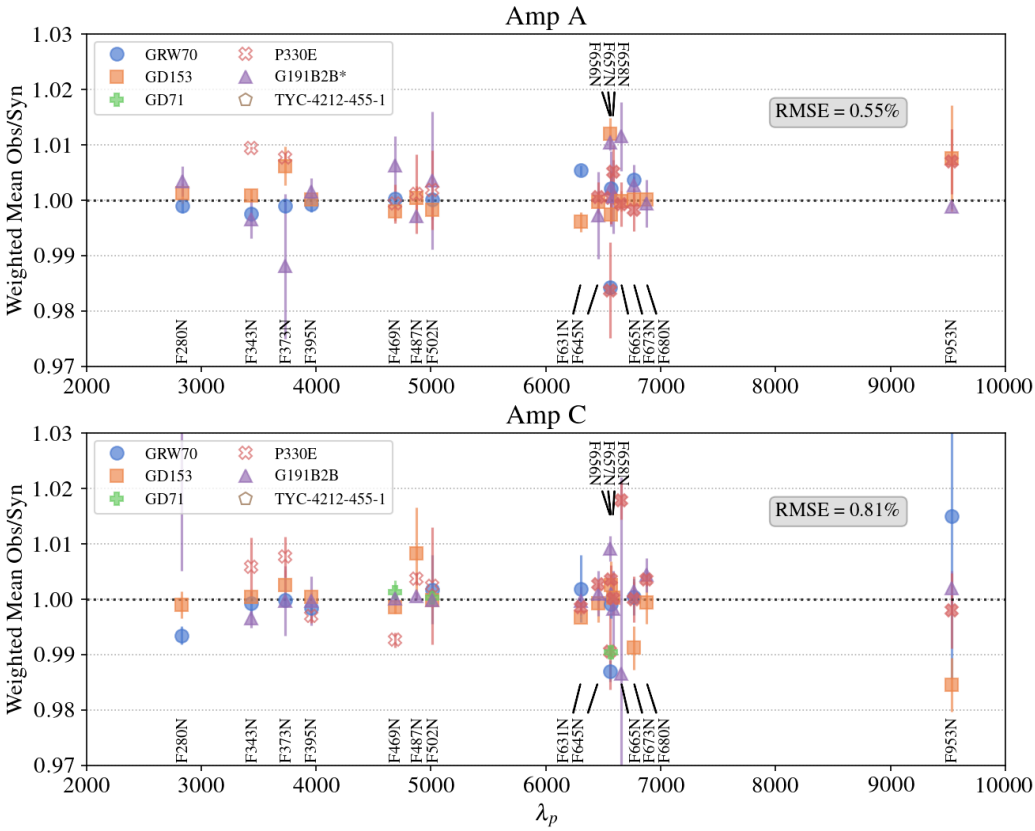

Figure 6: Weighted mean obs/syn flux ratio for amp A (top) and amp C (bottom) at the 2009 reference epoch (MJD=55008) as a function of filter pivot wavelength, for narrow-band filters.

treating the photometric solution as a global system of linear equations, rather than a series of pairwise comparisons, we ensure that stellar brightness estimates are anchored across the entire ensemble.

Figure 7 plots the magnitude residual (image - reference) for the top of UVIS1 and the bottom of UVIS2 as a function of date. To mitigate CTE effects, we compare only stars within 1024 rows of the readout amplifier on each detector. As these measurements are in delta magnitude, a positive slope yields increasing magnitudes (fainter fluxes) with time and a loss in sensitivity.

The updated UVIS1 slope -0.160 ± 0.002 %/yr is significantly shallower than the IMPHTTAB slope -0.213 ± 0.068 %/yr and closer to the updated UVIS2 slope (-0.161 ± 0.002 %/yr). For UVIS2, the updated slope value is consistent with the IMPHTTAB slope value of -0.171 ± 0.075 to within the uncertainties.

After detrending the cluster photometry the residuals have a standard deviation of 0.415% for UVIS1 and 0.279% for UVIS2. The best fit slopes differ slightly than the slopes presented in this document, with -0.143%/yr for UVIS1 and -0.187%/yr for UVIS2. The IMPHTTAB slope estimate of -0.213% per year in UVIS1 would significantly overestimate the sensitivity loss when applied to the clusters. When applied, this overestimation introduces a chip-

dependent photometric offset (PHTRATIO error) of nearly 1% at the current epoch in 2026. As these cluster measurements also show some nonlinearities in the sensitivity evolution (the first three years of data appear to show steeper sensitivity loss), the standard deviations are likely inflated compared to the actual photometric error.

While clusters are useful for monitoring TDS trends, CTE losses can introduce systematic uncertainties. The CALSPEC standards are observed in the corner subarrays, such that any CTE effects are negligible compared to the total flux (in electrons) of each star. The corners, on the other hand, have larger flat field uncertainties compared to the center of the detector. Additionally, the aperture correction maps used may introduce some bias into the photometry. As the aperture correction maps depend on the focus of the image, any error in focus measurement in the cluster photometry, or photometry used to create the maps can introduce systematic errors.

While a 5-pixel aperture was used to mitigate crowding effects, many of the stars are still affected by nearby neighbors. Given the long time baseline of the data, the random internal motion of stars in the cluster cause the contamination from nearby stars to change with time. Despite these potential systematic errors, the detrended relative photometric residuals show significantly less time evolution, indicating a significant improvement from applying the updated slopes.

5.2 White dwarf standard: GRW70

We demonstrate the improved agreement in the calculated flux of the same target measured on different detectors. To do this, we reprocess observations of the CALSPEC standard GRW70 in the F555W filter using the updated linear fits.

Figure 8 plots the total flux of the star as a function of date using the IMPHTTAB slope values in the top panel. For observations in late-2025, flux values of the same target on UVIS2 (in orange) are signficantly lower than the flux values on UVIS1 (in blue). With the updated slope values, the mean UVIS2 flux for GRW70 is consistent with the UVIS1 value to within the measurement uncertainties.

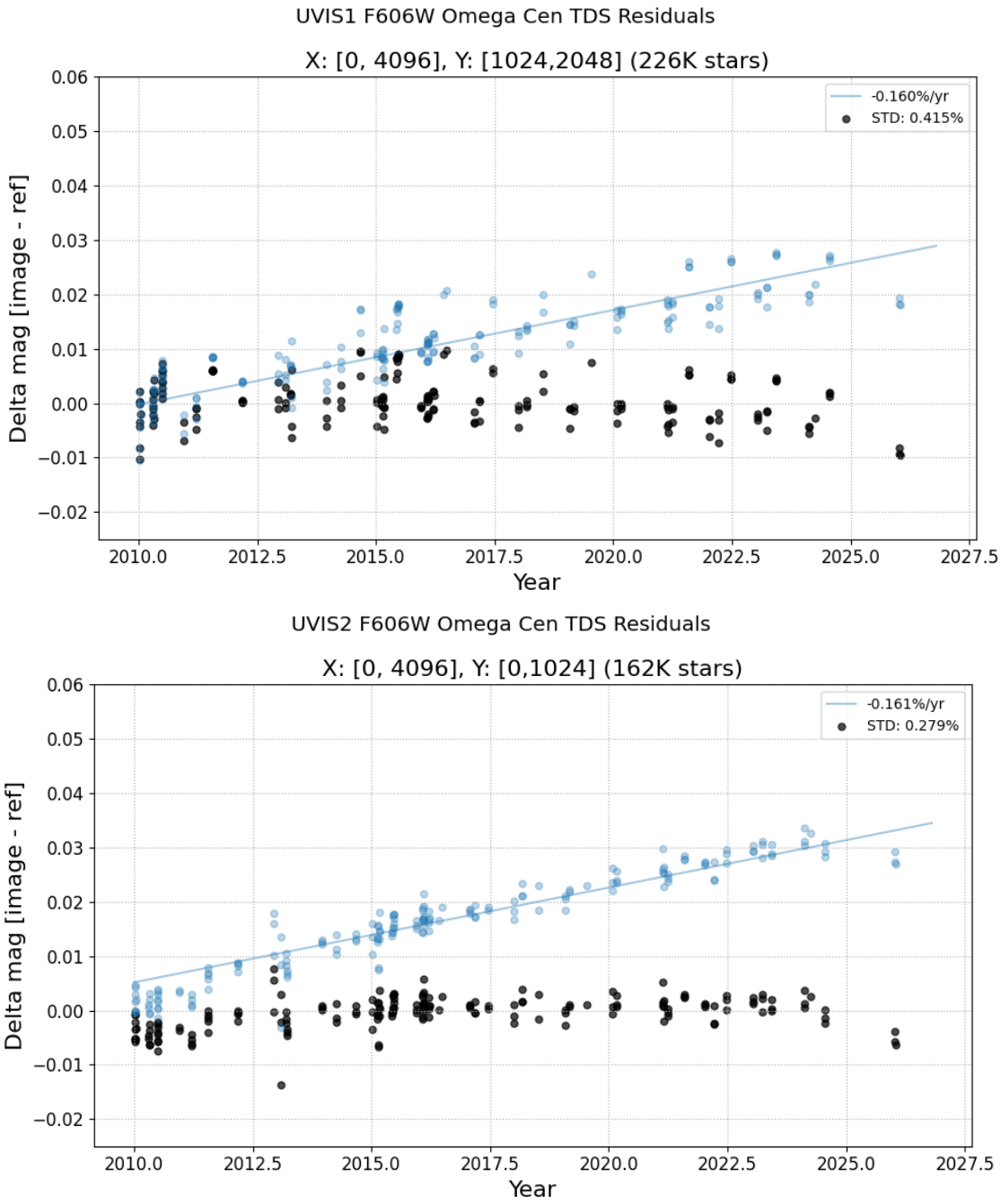

Figure 7: Relative photometry of the core of ω Cen in the F606W filter for UVIS1 (top) and UVIS2 (bottom). Blue symbols show the change in the observed magnitude (the image dependent offset calculated by least squares optimization to minimize the variance in measured flux across all stars), with slope values from Table 1 and Table 2 superimposed as a blue line. Black symbols show magnitude residuals after correcting by the new model slope values (subtracting the blue lines). The residuals center on zero change over time, indicating that the correction is accurately capturing the TDS. The best fit slopes are -0.143%/yr for UVIS1 and -0.187%/yr for UVIS2, which deviate from the computed slopes by less than 0.5% over the 16 year baseline for these observations.

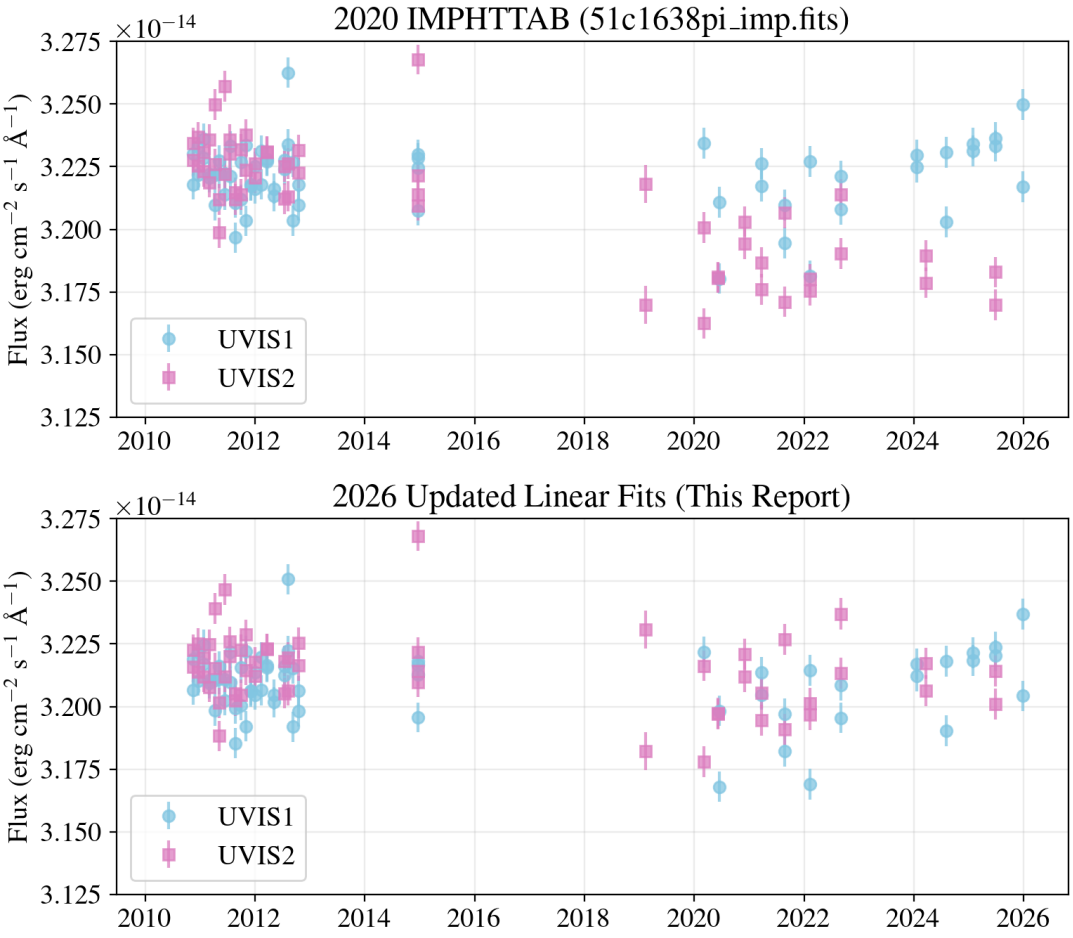

Figure 8: Flux values (in physical units) in the F555W filter for the CALSPEC white dwarf GRW70, where cyan symbols show observations on UVIS1 and pink symbols show UVIS2. The top panel shows the flux derived using inverse sensitivities values from the 2020 IMPHTTAB while the bottom panel shows flux values derived using the 2026 updated linear fits. For the most recent observations in November 2025, flux values in the top panel are 1.5% lower for UVIS2 than for UVIS1. With the new solution, flux values for the two detectors are in closer agreement over the WFC3 lifetime.

6 Conclusion

With new estimates of the UVIS EE by O'Connor et al. (2026) and $\sim$ 17 years of monitoring of CALSPEC standards, we compute updated linear fits to the observed photometry for all 42 imaging filters on UVIS1 and UVIS2, excluding quad filters and the UVIS grism. Results of this work are summarized below:

- **Intercept offsets are primarily due to EE improvements.** EE tables are used to correct 10-pixel aperture photometry to an 'infinite' aperture (6.″0). For a subset of

wide filters (F218W, F225W, F275W, F336W, F775W, F814W, F845M), the EE(10) values differ by $\approx 0.5 - 1.0\%$, with 1-2% differences for long-pass filters. A few narrow-band filters have intercept offsets exceeding 1%, but the linear fits are based on sparse datasets and have larger errors. The updated EE values improve the intercept of the linear fit at the 2009 reference epoch relative to the solution from Calamida et al. (2021), used to populate photometric keywords in the image headers.

- **A wavelength-dependence is noted in the sensitivity loss rates.** The observed count rates for UV filters (after 2011) are declining at nearly twice the rate of red filters, e.g. -0.2% per year for F225W versus -0.1% per year for F814W. Of the twelve wide-band filters, we find similar loss rates for UVIS1 and UVIS2 in five filters (F218W, F225W, F275W, F606W and F814W). For six filters (F390W, F438W, F475W, F555W, F625W, F775W), loss rates for UVIS1 are slightly larger than for UVIS2 (see filled circles in Figure 3).

- **For wide-band filters, the inverse sensitivity values differ by more than 1% in only a few cases.** Considering only the twelve popular wide filters, we identify several in which the updated inverse sensitivity values differ by more than 1.0% at any date between 2009 and 2026. These include three on UVIS1 (F218W, F606W, F625W) and five on UVIS2 (F218W, F225W, F390W, F555W, F625W). For differences exceeding 0.5%, we identify four filters on UVIS1 (F218W, F390W, F606W, F625W) and eleven on UVIS2 (F218W, F225W, F275W, F336W, F390W, F475W, F555W, F606W, F625W, F775W, F814W). These filters are highlighted in bold-face font in Tables 1, 2, 3, and 4.

- **The slopes for some filters are significantly improved, but the effects are often mitigated by their intercept.** UVIS2 monitoring did not begin until after 2014 for several stars, and the predicted loss rates for UVIS2 are significantly improved for a few filters: F336W, F390W, F475W, F555W, F625W. An example is shown in Figure 13, where the F475W UVIS2 slope (-0.150% yr^{-1}) is 2.5x steeper than the IMPHTTAB slope (-0.061% yr^{-1}). However, the positive intercept ($+0.58\%$) mitigates the effect so that the difference in the inverse sensitivity in mid-2026 is only $\sim 1\%$. For example: obs/syn$_{new} = 1.0058 - 0.00150\%/\mathrm{yr} \times 17$ yr $= 0.979$, obs/syn$_{old} = 1.0 - 0.00061\%/\mathrm{yr} \times 17$ yr $= 0.990$, and the difference (new-old) is -0.011.

- **The F775W inverse-sensitivity ratio (UVIS2/UVIS1) changes by 1.2% at the reference epoch.** A notable improvement is found in the combined intercept offset for F775W, where UVIS1 is +0.3% and the UVIS2 is -0.9%. This gives a total change of $\approx 1.2\%$ in the count rates between the chips for data in 2009 (Figure 4). This improves both the reference-epoch inverse sensitivity ratio (PHTRATIO$_{ref}$) and the time-evolved value (PHTRATIO$_{MJD}$), applied during the `FLUXCOR` step of `calwf3`.

- **The new slopes significantly reduce the RMS scatter in the obs/syn ratio.** The new slopes improve the RMS error of the obs/syn ratio for the five CALSPEC stars in wide and medium filters, from 0.5% for each detector in the photometric calibration by Calamida et al., to 0.31% for UVIS1 and 0.22% for UVIS2 using the

updated calibration. The RMS error for narrow-band filters is 0.55% for UVIS1 and 0.81% for UVIS2. However, errors for narrow-band filters may be underestimated, as inverse sensitivities are computed relative to the continuum flux of predominantly white dwarf stars, while emission line measurements must be calibrated using a different methodology (see section 7.3).

Future work may explore using additional line segments or a rolling average to account for changes in sensitivity over time. We will also compare our results with the slopes from UVIS scans of GD153 and GRW70 for a subset of wide filters using the same observation dates. Other work may include testing whether using CALSPEC models (or updated SEDs) improves the agreement in the obs/syn ratio between stars, for example measuring the specific contributions to the calibration from P330E and GRW70, which are not used for the photometric calibration of the ACS CCD cameras described in Bohlin et al. (2020b).

7 Recommendations

New UVIS photometric zeropoints (STMAG, ABMAG, VEGAMAG) will be published as an Addendum to this report upon delivery of an updated IMPHTTAB reference file (and synphot throughput curves). In the interim, we provide a workflow to correct photometry derived from FLC images calibrated with the 2020 IMPHTTAB, *51c1638pi_imp.fits*.

Currently this method is recommended for observations at a single observing epoch, as described in section 7.1. For multi-epoch observations of the same target, users may wish to correct the observed countrates of each UVIS detector for a given FLC image before combining the observations (see section 7.2). For emission line-filters, the updated TDS solutions can be used to correct for changes in the relative sensitivity with time (or between chips) but are not recommended for absolute photometry (see section 7.3).

7.1 Correcting Photometric Observations

We present new time-dependent inverse sensitivity values for all 42 imaging filters on both WFC3/UVIS detectors. We recommend using the new linear fits to correct existing UVIS photometry at any specific observation date.

In the tables of Appendix A, we highlight filters for which applying these updated values would affect the result by more than 0.5% (W, M), 1.0% (LP, X), and 1.5% (N) at any time between 2009 at 2026. LP, X, and N filters have broader thresholds due to sparser datasets and larger uncertainties in the fit. **WFC3 users who would like to update absolute photometry using these new models can find instructions in Appendix B**.

Filters with intercept offsets on a single UVIS detector will have changes in the inverse sensitivity *ratio* at the reference epoch, $\mathrm{PHTRATIO}_{ref}$. This ratio is important for a proper time-evolution to the current epoch, $\mathrm{PHTRATIO}_{MJD}$, using the model slopes for each detector and ensures that FLC observations will have the same count rates on both chips after the `FLUXCORR` step of `calwf3` for a given target.

7.2 Combining Multi-Epoch Observations

For observations spanning multiple epochs, users may wish to correct for changes in the observed countrates before combining the FLC images with `AstroDrizzle` [6]. For example, for F225W images acquired 5 years apart, the observed count rates decrease by $\approx 1\%$. For these cases, users may wish to simply wait for new FLC products in MAST, expected late-2026 with the delivery of an updated IMPHTTAB reference file. Once those products are available, users may follow the tutorial on drizzling multi-epoch datasets: **WFC3/UVIS Time-dependent Photometry**[7] in the HST notebooks repository[8].

7.3 Emission Line Calibration

WFC3's narrow-band filters may be used to study emission-line objects such as planetary nebulae or supernova remnants. To derive emission-line fluxes, the inverse sensitivity values in the image header are not recommended for absolute calibration. Instead, users should correct the observed flux for signal arising from the underlying continuum and any contaminating lines. A method to carry out this correction is described in Section 9.1.8 of the WFC3 Data Handbook.

Acknowledgments

We thank WFC3 team members M. Revalski and P. R. McCullough for their reviews of this report and suggestions to improve the content. We are grateful to R. C. Bohlin and A. Calamida for helpful discussions about absolute photometric calibration. We thank M. Marinelli for testing the new filter throughput curves and aperture correction files for synphot and A. O'Connor and N. Grogin from the WFC3 Photometry Team for supporting this work.

This work made use of:

- Astropy, a community-developed core Python package and an ecosystem of tools and resources for astronomy
- Photutils, an Astropy package for detection and photometry of astronomical sources
- The CALSPEC database for flux standards on the HST system.
- The SIMBAD database, operated at CDS, Strasbourg, France

[6] `https://drizzlepac.readthedocs.io/en/latest/getting-started.html`

[7] `https://spacetelescope.github.io/hst_notebooks/notebooks/WFC3/uvis_time_dependent_photometry/uvis_timedep_phot.html`

[8] `https://spacetelescope.github.io/hst_notebooks/notebooks/WFC3/README.html`

References

Anderson, J. 2022, **One-Pass HST Photometry with hst1pass**, Instrument Science Report WFC3 2022-5

Avila, R. J., Chiaberge, M., Kossakowski, D., Averbukh, J., & Lockwood, S. 2019, **SBC Time-Dependent Sensitivity and L-flats**, Instrument Science Report ACS 2019-04

Bohlin, R. C., Gordon, K. D., & Tremblay, P. E. 2014, PASP, 126, 711, **Techniques and Review of Absolute Flux Calibration from the Ultraviolet to the Mid-Infrared**, doi: 10.1086/677655

Bohlin, R. C., Hubeny, I., & Rauch, T. 2020a, AJ, 160, 21, **New Grids of Pure-hydrogen White Dwarf NLTE Model Atmospheres and the HST/STIS Flux Calibration**, doi: 10.3847/1538-3881/ab94b4

Bohlin, R. C., Ryon, J. E., & Anderson, J. 2020b, **Update of the Photometric Calibration of the ACS CCD Cameras**, Instrument Science Report ACS 2020-08

Calamida, A., Mack, J., Medina, J., et al. 2021, **New Time-dependent WFC3 UVIS Inverse Sensitivities**, Instrument Science Report WFC3 2021-04

Carlberg, J. K., & Monroe, T. 2017, **Updated Time Dependent Sensitivity Corrections for STIS Spectral Modes**, Instrument Science Report STIS 2017-06

Deustua, S. E., Mack, J., Bowers, A. S., et al. 2016, **UVIS 2.0 Chip-dependent Inverse Sensitivity Values**, Instrument Science Report WFC3 2016-03

Gosmeyer, C. M., Baggett, S., Deustua, S., & Hammer, D. M. 2014, **Update on the WFC3/UVIS Stability and Contamination Monitor**, Instrument Science Report WFC3 2014-20

Hartig, G. F. 2009, **WFC3 SMOV Programs 11436/8: UVIS On-orbit PSF Evaluation**, Instrument Science Report WFC3 2009-38

Huynh, K., Bajaj, V., Mack, J., & Calamida, A. 2025, **Improved UVIS Aperture Corrections derived from Focus Diverse PSF Maps**, Instrument Science Report WFC3 2025-05, doi: 10.48550/arXiv.2510.23435

Huynh, K., & McCullough, P. R. 2023, **UVIS Shutter Timing Jitter**, Instrument Science Report WFC3 2023-04

Kalirai, J. S., Cox, C., Dressel, L., et al. 2010, **WFC3 Pixel Area Maps**, Instrument Science Report WFC3 2010-08

Kalirai, J. S., MacKenty, J., Rajan, A., et al. 2009, **WFC3 SMOV Proposal 11450: The Photometric Performance and Calibration of WFC3/UVIS**, Instrument Science Report WFC3 2009-31

Khandrika, H., Deustua, S., & Mack, J. 2018, **WFC3/UVIS - Temporal and Spatial Variations in Photometry**, Instrument Science Report WFC3 2018-16

O'Connor, A., Mack, J., & Bajaj, V. 2026, **Updates to WFC3/UVIS Encircled Energy Values in Select Filters**, Instrument Science Report WFC3 2026-02

Pagul, A., & Rivera, I. 2024, **WFC3 Data Handbook, Version 6.0**

Shanahan, C. E., Gosmeyer, C. M., & Baggett, S. 2017, **2017 Update on the WFC3/UVIS Stability and Contamination Monitor**, Instrument Science Report WFC3 2017-15

Stetson, P. B. 1987, PASP, 99, 191, **DAOPHOT: A Computer Program for Crowded-Field Stellar Photometry**, doi: 10.1086/131977

Appendix A: Updated Inverse Sensitivity Values

The tables in this appendix provide the new linear best-fit coefficients (slope and intercept) and the new reference-epoch inverse sensitivity values ($\mathrm{PHOTFLAM_{ref}}$ for UVIS1 or $\mathrm{PHTFLAM2_{ref}}$ for UVIS2) for all 42 imaging filters (excluding quad filters). These tables can be used along with the method in section 7.3 to manually correct UVIS photometry until a new IMPHTTAB reference file is delivered in mid-2026.

Table 1: UVIS1 linear best-fit coefficients for visible-wavelength filters and new reference epoch inverse sensitivity values. The Intercept Offset column lists the percent difference in the model y-intercept from 100%, i.e. percent difference from obs/syn = 1.0 from the 2020 IMPHTTAB value at MJD 55008. Filters in bold font have a predicted change in flux which differs from the 2020 IMPHTTAB prediction by more than 0.5% (wide, medium), 1.0% (LP, X), or 1.5% (narrow) for any date between 2009 and 2026. Filters marked with an asterisk have fits constrained by the F625W filter slope, rather than a weighted mean of individual-target slopes.

Filter	λ_p (Å)	Slope (% yr^{-1})	Intercept Offset (%)	PHOTFLAM$_{\rm ref}$ (erg cm^{-2} Å^{-1} e^{-1})
F336W	3354.5	-0.073 ± 0.003	0.36 ± 0.02	$(1.281 \pm 0.002) \times 10^{-18}$
F390W	3923.7	-0.141 ± 0.003	0.20 ± 0.02	$(5.007 \pm 0.015) \times 10^{-19}$
F438W	4326.2	-0.146 ± 0.003	0.24 ± 0.02	$(6.743 \pm 0.038) \times 10^{-19}$
F475W	4773.1	-0.174 ± 0.003	0.34 ± 0.02	$(2.490 \pm 0.012) \times 10^{-19}$
F555W	5308.4	-0.176 ± 0.003	0.34 ± 0.02	$(1.826 \pm 0.005) \times 10^{-19}$
F606W	5889.2	-0.160 ± 0.002	0.28 ± 0.02	$(1.150 \pm 0.014) \times 10^{-19}$
F625W	6242.6	-0.128 ± 0.005	0.65 ± 0.06	$(1.711 \pm 0.015) \times 10^{-19}$
F775W	7651.4	-0.105 ± 0.005	0.31 ± 0.05	$(2.087 \pm 0.009) \times 10^{-19}$
F814W	8039.1	-0.118 ± 0.003	0.11 ± 0.02	$(1.496 \pm 0.010) \times 10^{-19}$
F390M	3897.2	-0.147 ± 0.005	-0.20 ± 0.03	$(2.556 \pm 0.012) \times 10^{-18}$
F410M	4109.0	-0.130 ± 0.006	-0.40 ± 0.07	$(2.359 \pm 0.008) \times 10^{-18}$
F467M	4682.6	-0.161 ± 0.004	-0.55 ± 0.04	$(1.663 \pm 0.010) \times 10^{-18}$
F547M	5447.5	-0.156 ± 0.004	0.42 ± 0.03	$(4.577 \pm 0.042) \times 10^{-19}$
F621M	6218.9	-0.117 ± 0.004	0.15 ± 0.05	$(4.016 \pm 0.026) \times 10^{-19}$
F689M	6876.8	-0.136 ± 0.008	-0.04 ± 0.06	$(3.725 \pm 0.010) \times 10^{-19}$
F763M	7614.4	-0.052 ± 0.008	-0.44 ± 0.09	$(3.847 \pm 0.024) \times 10^{-19}$
F845M	8439.1	-0.052 ± 0.007	-1.56 ± 0.08	$(4.596 \pm 0.039) \times 10^{-19}$
F343N	3435.2	-0.055 ± 0.009	0.02 ± 0.09	$(2.571 \pm 0.004) \times 10^{-18}$
F373N	3730.2	-0.11 ± 0.02	-0.0 ± 0.1	$(1.350 \pm 0.011) \times 10^{-17}$
F395N	3955.2	-0.154 ± 0.008	0.04 ± 0.09	$(5.959 \pm 0.014) \times 10^{-18}$
F469N	4688.1	-0.20 ± 0.02	-0.39 ± 0.06	$(9.335 \pm 0.026) \times 10^{-18}$
F487N	4871.4	-0.19 ± 0.02	0.3 ± 0.2	$(5.878 \pm 0.025) \times 10^{-18}$
F502N	5009.6	-0.152 ± 0.009	-1.13 ± 0.05	$(5.148 \pm 0.024) \times 10^{-18}$
F631N*	6304.3	-0.11 ± 0.03	0.8 ± 0.4	$(4.786 \pm 0.054) \times 10^{-18}$
F645N	6453.6	-0.11 ± 0.02	0.6 ± 0.2	$(3.290 \pm 0.013) \times 10^{-18}$
F656N	6561.4	-0.12 ± 0.02	0.3 ± 0.3	$(1.709 \pm 0.060) \times 10^{-17}$
F657N	6566.6	-0.09 ± 0.01	-0.3 ± 0.2	$(2.187 \pm 0.009) \times 10^{-18}$
F658N*	6584.0	-0.1 ± 0.2	1.6 ± 0.5	$(9.592 \pm 0.160) \times 10^{-18}$
F665N	6655.9	-0.14 ± 0.02	-0.2 ± 0.1	$(1.984 \pm 0.018) \times 10^{-18}$
F673N	6765.9	-0.10 ± 0.01	-0.5 ± 0.1	$(2.203 \pm 0.014) \times 10^{-18}$
F680N	6877.6	-0.1 ± 0.1	-1.4 ± 0.4	$(6.930 \pm 0.095) \times 10^{-19}$
F953N	9530.6	-0.08 ± 0.03	-0.0 ± 0.3	$(8.104 \pm 0.086) \times 10^{-18}$
F200LP	4971.9	-0.190 ± 0.005	2.17 ± 0.05	$(5.015 \pm 0.059) \times 10^{-20}$
F475X	4940.7	-0.19 ± 0.02	0.57 ± 0.09	$(1.529 \pm 0.003) \times 10^{-19}$
F350LP	5873.9	-0.145 ± 0.003	0.48 ± 0.02	$(5.141 \pm 0.024) \times 10^{-20}$
F600LP	7468.1	-0.107 ± 0.008	0.21 ± 0.06	$(8.643 \pm 0.055) \times 10^{-20}$
F850LP	9176.1	-0.091 ± 0.004	2.06 ± 0.03	$(3.634 \pm 0.022) \times 10^{-19}$

Table 2: Same as Table 1, but for UVIS2. Filters marked with an asterisk have fits constrained by the F625W filter slope, except for F763M which was constrained by the F775W filter slope.

Filter	λ_p (Å)	Slope (% yr^{-1})	Intercept Offset (%)	PHTFLAM2$_{\rm ref}$ (erg cm^{-2} Å^{-1} e^{-1})
F336W	3354.7	-0.103 ± 0.003	0.86 ± 0.03	$(1.243 \pm 0.003) \times 10^{-18}$
F390W	3920.7	-0.122 ± 0.003	0.18 ± 0.03	$(4.976 \pm 0.008) \times 10^{-19}$
F438W	4325.1	-0.135 ± 0.003	0.37 ± 0.03	$(6.753 \pm 0.021) \times 10^{-19}$
F475W	4772.2	-0.150 ± 0.003	0.58 ± 0.03	$(2.503 \pm 0.011) \times 10^{-19}$
F555W	5307.9	-0.146 ± 0.004	0.50 ± 0.04	$(1.846 \pm 0.013) \times 10^{-19}$
F606W	5887.7	-0.161 ± 0.002	0.46 ± 0.02	$(1.158 \pm 0.009) \times 10^{-19}$
F625W	6242.0	-0.109 ± 0.004	0.29 ± 0.05	$(1.718 \pm 0.008) \times 10^{-19}$
F775W	7648.3	-0.062 ± 0.005	-0.90 ± 0.05	$(2.134 \pm 0.013) \times 10^{-19}$
F814W	8029.3	-0.118 ± 0.002	-0.49 ± 0.02	$(1.531 \pm 0.008) \times 10^{-19}$
F390M	3897.0	-0.153 ± 0.005	0.07 ± 0.04	$(2.512 \pm 0.009) \times 10^{-18}$
F410M	4108.9	-0.144 ± 0.006	0.56 ± 0.08	$(2.340 \pm 0.007) \times 10^{-18}$
F467M	4682.6	-0.191 ± 0.004	-0.30 ± 0.03	$(1.651 \pm 0.004) \times 10^{-18}$
F547M	5447.2	-0.158 ± 0.003	0.15 ± 0.02	$(4.572 \pm 0.021) \times 10^{-19}$
F621M	6219.2	-0.068 ± 0.006	-0.35 ± 0.07	$(4.058 \pm 0.025) \times 10^{-19}$
F689M	6876.5	-0.13 ± 0.01	-0.4 ± 0.1	$(3.771 \pm 0.035) \times 10^{-19}$
F763M*	7612.7	-0.05 ± 0.01	-0.6 ± 0.1	$(3.928 \pm 0.032) \times 10^{-19}$
F845M	8437.3	-0.064 ± 0.008	-1.33 ± 0.08	$(4.626 \pm 0.052) \times 10^{-19}$
F343N	3435.2	-0.045 ± 0.009	-0.3 ± 0.1	$(2.492 \pm 0.010) \times 10^{-18}$
F373N	3730.2	-0.10 ± 0.02	-0.2 ± 0.1	$(1.318 \pm 0.006) \times 10^{-17}$
F395N	3955.2	-0.116 ± 0.009	-0.3 ± 0.1	$(5.965 \pm 0.020) \times 10^{-18}$
F469N	4688.1	-0.17 ± 0.02	-1.07 ± 0.05	$(9.365 \pm 0.077) \times 10^{-18}$
F487N	4871.4	-0.19 ± 0.03	-1.6 ± 0.4	$(5.915 \pm 0.093) \times 10^{-18}$
F502N	5009.6	-0.139 ± 0.007	-0.67 ± 0.04	$(5.147 \pm 0.023) \times 10^{-18}$
F631N*	6304.3	-0.10 ± 0.02	0.6 ± 0.4	$(4.772 \pm 0.048) \times 10^{-18}$
F645N*	6453.6	-0.1 ± 0.1	0.4 ± 0.5	$(3.313 \pm 0.021) \times 10^{-18}$
F656N*	6561.4	-0.12 ± 0.03	0.9 ± 0.4	$(1.646 \pm 0.020) \times 10^{-17}$
F657N	6566.6	-0.09 ± 0.02	-0.2 ± 0.2	$(2.187 \pm 0.011) \times 10^{-18}$
F658N	6583.9	-0.16 ± 0.03	0.9 ± 0.3	$(9.572 \pm 0.074) \times 10^{-18}$
F665N*	6655.8	-0.1 ± 0.1	-1.3 ± 0.5	$(2.030 \pm 0.015) \times 10^{-18}$
F673N*	6765.9	-0.10 ± 0.02	0.7 ± 0.4	$(2.228 \pm 0.026) \times 10^{-18}$
F680N	6877.4	-0.12 ± 0.09	0.3 ± 0.4	$(6.949 \pm 0.050) \times 10^{-19}$
F953N	9530.5	-0.05 ± 0.03	0.3 ± 0.4	$(8.395 \pm 0.100) \times 10^{-18}$
F200LP	4875.1	-0.172 ± 0.006	-0.21 ± 0.05	$(5.124 \pm 0.060) \times 10^{-20}$
F475X	4937.4	-0.16 ± 0.03	0.8 ± 0.1	$(1.533 \pm 0.007) \times 10^{-19}$
F350LP	5851.1	-0.170 ± 0.006	1.12 ± 0.07	$(5.288 \pm 0.023) \times 10^{-20}$
F600LP	7453.7	-0.14 ± 0.01	0.33 ± 0.09	$(8.866 \pm 0.073) \times 10^{-20}$
F850LP	9169.9	-0.112 ± 0.004	2.39 ± 0.04	$(3.783 \pm 0.026) \times 10^{-19}$

Table 3: UVIS1 linear best-fit coefficients for UV-wavelength filters. Two line segments are fit to each filter, one for MJD $<$ 55738, and one for MJD $\geq$ 55738. Certain filters with large differences from the 2020 IMPHTTAB values are shown in bold, as in Tables 1 and 2. Filters marked with an asterisk have fits constrained by the F275W filter slope. Inverse sensitivity values for both segments are at the reference epoch MJD=55008; i.e. the values for the second segment are projected back to that date.

	Filter	λ_p (Å)	Slope (% yr^{-1})	Intercept Offset (%)	PHOTFLAM$_{\rm ref}$ (erg cm^{-2} Å^{-1} e^{-1})
MJD $<$ 55738	**F218W**	2228.0	0.69 ± 0.02	-1.23 ± 0.03	$(1.485 \pm 0.010) \times 10^{-17}$
	F225W	2372.1	0.41 ± 0.02	-0.34 ± 0.03	$(4.601 \pm 0.006) \times 10^{-18}$
	F275W	2709.7	0.15 ± 0.02	-0.26 ± 0.03	$(3.231 \pm 0.005) \times 10^{-18}$
	F300X*	2820.5	0.84 ± 0.06	-0.28 ± 0.09	$(1.419 \pm 0.003) \times 10^{-18}$
	F280N*	2832.9	0.95 ± 0.2	-1.0 ± 0.1	$(5.879 \pm 0.046) \times 10^{-17}$
MJD $\geq$ 55738	**F218W**	2228.0	-0.235 ± 0.003	0.61 ± 0.05	$(1.446 \pm 0.010) \times 10^{-17}$
	F225W	2372.1	-0.199 ± 0.003	0.88 ± 0.05	$(4.524 \pm 0.006) \times 10^{-18}$
	F275W	2709.7	-0.161 ± 0.003	0.36 ± 0.04	$(3.203 \pm 0.005) \times 10^{-18}$
	F300X	2820.5	-0.151 ± 0.009	1.7 ± 0.1	$(1.390 \pm 0.003) \times 10^{-18}$
	F280N	2832.9	-0.15 ± 0.04	1.2 ± 0.5	$(5.749 \pm 0.045) \times 10^{-17}$

Table 4: Same as Table 3, but for UVIS2 UV-wavelength filters

	Filter	λ_p (Å)	Slope (% yr^{-1})	Intercept Offset (%)	PHTFLAM2$_{\rm ref}$ (erg cm^{-2} Å^{-1} e^{-1})
MJD $<$ 55738	**F218W**	2223.7	0.60 ± 0.02	-0.98 ± 0.04	$(1.156 \pm 0.011) \times 10^{-17}$
	F225W	2358.4	0.62 ± 0.02	-1.15 ± 0.04	$(3.852 \pm 0.005) \times 10^{-18}$
	F275W	2703.3	0.39 ± 0.03	-0.72 ± 0.06	$(3.075 \pm 0.006) \times 10^{-18}$
	F300X*	2805.8	1.36 ± 0.06	-1.5 ± 0.1	$(1.338 \pm 0.014) \times 10^{-18}$
	F280N*	2830.0	0.3 ± 0.2	-0.2 ± 0.1	$(5.783 \pm 0.096) \times 10^{-17}$
MJD $\geq$ 55738	**F218W**	2223.7	-0.238 ± 0.002	0.70 ± 0.05	$(1.119 \pm 0.011) \times 10^{-17}$
	F225W	2358.4	-0.211 ± 0.002	0.51 ± 0.04	$(3.741 \pm 0.004) \times 10^{-18}$
	F275W	2703.3	-0.164 ± 0.003	0.39 ± 0.05	$(3.016 \pm 0.006) \times 10^{-18}$
	F300X	2805.8	-0.155 ± 0.009	1.5 ± 0.1	$(1.313 \pm 0.014) \times 10^{-18}$
	F280N	2830.0	-0.17 ± 0.04	0.6 ± 0.5	$(5.648 \pm 0.094) \times 10^{-17}$

Appendix B: Manually Updating UVIS Photometry

1. Method

Users who wish to update existing UVIS photometry using the new TDS models may do so without re-running the `calwf3` calibration pipeline by using the following steps.

1. Compute photometric measurements in units of e^-/s. Such measurements may be taken from a calibrated, CTE-corrected UVIS image (FLC) that has been multiplied by the Pixel Area Map (PAM) and divided by its exposure time.

2. For targets observed on UVIS2, divide the measured countrate (in e^-/s) by the value of the PHTRATIO keyword from the image SCI header. This 'backs out' the FLUXCORR step performed by `calwf3`, which is described further in the WFC3 Data Handbook, Section 3.2.13.[9]. **This step should be skipped for UVIS1 photometry.**

$$\begin{cases} \text{UVIS2} \rightarrow \text{Divide countrate by PHTRATIO} \\ \text{UVIS1} \rightarrow \text{Leave countrate unchanged} \end{cases}$$

3. Identify the new inverse sensitivity (either PHOTFLAM_{ref} or PHTFLAM2_{ref}), slope, and intercept values from Table 1, 2, 3, or 4 for the filter and UVIS detector with which your measurement was taken. For UV filters, ensure you are using values from the appropriate epoch for your observation date.

4. Calculate the inverse sensitivity for your observation date using the updated reference-epoch inverse sensitivity, slope, and intercept for your observation:

$$\text{PHOTFLAM}_{MJD} = \frac{\text{PHOTFLAM}_{ref}}{1 + S \div I \times \Delta t} \tag{1}$$

   where S is the slope in units of yr^{-1}, derived from the tabulated value by dividing by 100%; I is the unitless intercept, derived the tabulated value by dividing by 100% and adding 1; and Δt is the time in years between the observation and the reference epoch (MJD=55008), i.e. $\Delta t = (\text{MJD-MJD}_{ref})/365.25$.

5. The flux for a UVIS observation is calculated from the countrate, measured in an aperture of radius r using the following equation.

$$F_\lambda = \frac{CR_r \times \text{PHOTFLAM}_{MJD}}{EE_r} \tag{2}$$

   The corrected PHOTFLAM_{MJD} can be used to calculate the flux for your observation with Equation 2, where EE_r is the encircled energy for radius r from O'Connor et al.

[9] `https://hst-docs.stsci.edu/wfc3dhb/chapter-3-wfc3-data-calibration/3-2-uvis-data-calibration-steps#id-3.2UVISDataCalibrationSteps-3.2.133.2.13FluxnormalizationforUVIS1andUVIS2`

(2026). To work in magnitudes, the flux can be converted following the method in section 9.1.1 of the WFC3 Data Handbook [10] (Pagul & Rivera, 2024).

2. Worked Examples

UVIS2 Photometry

As an example, we walk through the procedure for correcting aperture photometry and obtaining a flux measurement for the white dwarf standard GRW70 observed in dataset `ifi556hrq_flc.fits`. The image was acquired in the F475W filter in HST program 17681 using the UVIS2-C512C-SUB aperture, which is in the lower-left corner of UVIS2. The MJD EXPSTART for the image is 60752.2 (March 2025) and the exposure time is 1.5 seconds.

1. Multiplying the FLC subarray image by the appropriate region of the PAM and dividing the image by the exposure time, we measure the countrate for our target in a 10-pixel aperture radius and then subtract the sigma-clipped mean sky background (per pixel) measured in an annulus between 156 and 165 pixels.

   This gives a countrate value within the aperture, CR_r = **154,467** e^-/s . Using the PHTFLAM2 value from the header (2.554×10^{-19} erg cm^{-2} Å^{-1} e^{-1}) and the EE at 10 pixels (**0.909**), we would compute a total flux for the source using the old correction:

   $F_{\lambda,old} = (CR_r * \text{PHTFLAM2})/EE_r = 4.340 \times 10^{-14}$ erg s^{-1} cm^{-2} Å^{-1}

2. Since this is a UVIS2 image, we divide our countrate by the PHTRATIO value in the SCI header (0.995194) to get the countrate of **155,213** e^-/s before FLUXCORR.

3. Using values from Table 2, we obtain a corrected PHTFLAM2 value from Equation 1:

$$\begin{aligned}
\text{PHTFLAM2}_{ref} &= 2.503 \times 10^{-19} \text{ erg cm}^{-2} \text{ Å}^{-1} \text{ e}^{-1} \\
\text{Slope} &= -0.150\% \text{ yr}^{-1} \Rightarrow S = -0.150\% \text{ yr}^{-1}/100\% = -0.00150 \text{ yr}^{-1} \\
\text{Intercept offset} &= 0.58\% \Rightarrow I = (1 + (0.58\%/100\%) = 1.0058 \\
\Delta t &= (60752 \text{ d} - 55008 \text{ d})/365.25 \text{ d yr}^{-1}) = 15.7 \text{ yr}
\end{aligned}$$

$$\begin{aligned}
\text{PHTFLAM2}_{MJD} &= \text{PHTFLAM2}_{ref}/(1 + (S/I) * \Delta t) \\
&= 2.503 \times 10^{-19}/(1 + (-0.00150/1.0058) * (15.7) \\
&= \boxed{2.563 \times 10^{-19} \text{ erg cm}^{-2} \text{ Å}^{-1} \text{ e}^{-1}}
\end{aligned}$$

4. With the new PHTFLAM2_{MJD} value, the measured UVIS2 countrate of 155,213 e^-/s, and the 10-pixel EE fraction of 0.909 from O'Connor et al.; the UVIS2 flux for the target is computed with Equation 2 as:

[10] `https://hst-docs.stsci.edu/wfc3dhb/chapter-9-wfc3-data-analysis/9-1-photometry#id-9.1Photometry-9.1.19.1.1PhotometricSystems`

$$F_{\lambda,new} = \frac{CR_r * PHTFLAM2_{MJD}}{EE_r}$$
$$= \boxed{4.376 \times 10^{-14} \text{ erg s}^{-1} \text{ cm}^{-2} \text{ Å}^{-1}}$$

This gives a flux ratio for UVIS2: $F_{\lambda,new}/F_{\lambda,old} = \mathbf{1.008}$; the observed flux is now brighter than calculated with the prior model.

UVIS1 Photometry

For comparison, we examine photometry of the same target in dataset `ifi505gdq_flc.fits`, observed on UVIS1 in program 17681 (F475W, 1.5 seconds) on MJD 60702 (Jan 2025), about 2 months prior to the UVIS1 image. The corrected photometry should give similar flux values for the two UVIS chips.

1. Multiplying the FLC subarray by the appropriate region of the PAM and dividing by the exposure time, we measure the countrate in a 10-pixel aperture radius and subtract the sigma-clipped mean sky in an annulus between 156 and 165 pixels.

   This gives a countrate value within the aperture, $CR_r = \mathbf{155{,}195}$ e$^-$/s. Using the PHOTFLAM value from the header (2.553×10^{-19} erg cm^{-2} Å^{-1} e^{-1}) and the EE at 10 pixels (**0.908**), we would compute a total flux for the source using the old correction:

   $F_{\lambda,old} = (CR_r * \text{PHOTFLAM})/EE_r = 4.364 \times 10^{-14}$ erg s^{-1} cm^{-2} Å^{-1}

2. Since this is a UVIS1 image, we do not apply a PHTRATIO correction to the observed count rate, CR.

3. Using values from Table 1, we obtain a corrected PHOTFLAM value from Equation 1:

$$\text{PHOTFLAM}_{ref} = 2.490 \times 10^{-19} \text{ erg cm}^{-2} \text{ Å}^{-1} \text{ e}^{-1}$$
$$S = -0.00174 \text{ yr}^{-1}$$
$$I = 1.0034$$
$$\Delta t = 15.6 \text{ yr}$$

$$\text{PHOTFLAM}_{MJD} = \text{PHOTFLAM}_{ref}/(1 + (S/I) * \Delta t)$$
$$= \boxed{2.559 \times 10^{-19} \text{ erg cm}^{-2} \text{ Å}^{-1} \text{ e}^{-1}}$$

4. With the new PHOTFLAM_{MJD} value, the UVIS1 countrate of 155,195 e$^-$/s, and the 10-pixel EE fraction of 0.908; the UVIS1 flux for the target is computed with Equation 2 as:

$$F_{\lambda,new} = \frac{CR_r * PHOTFLAM_{MJD}}{EE_r}$$
$$= \boxed{4.374 \times 10^{-14} \text{ erg s}^{-1} \text{ cm}^{-2} \text{ Å}^{-1}}$$

This gives a flux ratio for UVIS1: $F_{\lambda.new}/F_{\lambda,old}$ = **1.002**; the observed photometry is nearly identical to the value predicted with the prior model. The UVIS1 flux is also very close to the updated UVIS2 flux value computed above.

Appendix C: Obs/Syn Plots for Additional Filters and Model Fits for Individual-Targets

Obs/syn photometry plots for several commonly-used filters are provided for reference. These highlight the different cadence of observations for each target on UVIS1 versus UVIS2 for a given filter.

Model parameters (slopes and intercepts and the corresponding errors) for individual target fits are provided in Tables 5 and 6 for UVIS1 and UVIS2. These fits provide an initial TDS slope (and bounding box, $\pm 3\sigma$) as input for the combined fit for each filter (and detector chip), as described in subsection 3.1. The tables are particularly useful for showing which stars have the most weight in the combined fit. While P330E is used to derive slopes for all UVIS filters, it is not used in the combined fit for the intercept for blue filters with $\lambda_p < 5880$ Å, similar to the approach taken by (Calamida et al., 2021).

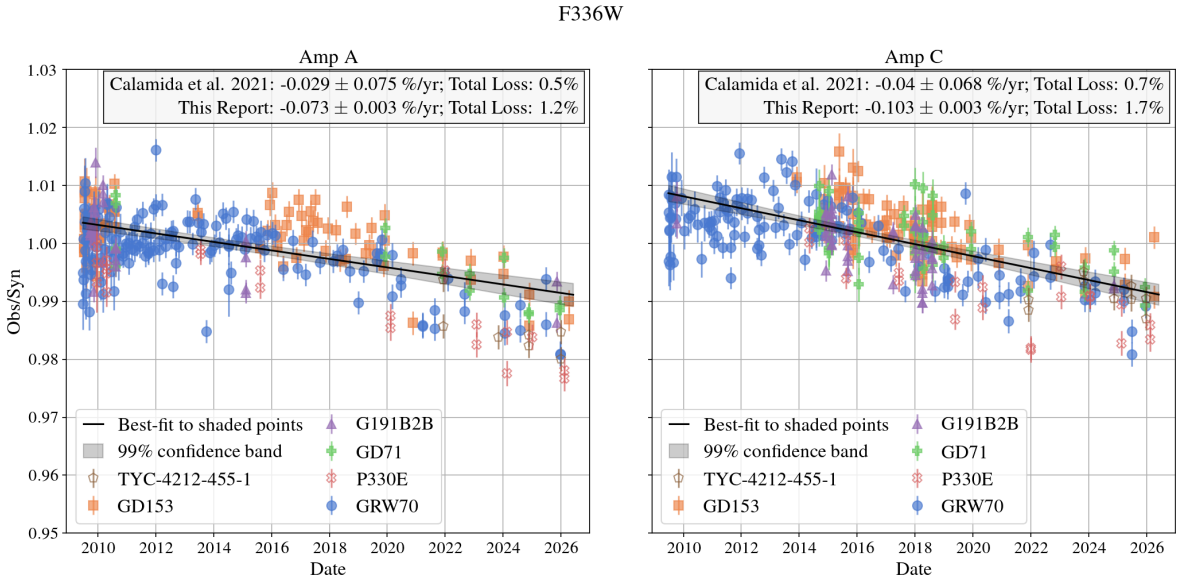

Figure 9: The same as Figure 1, but for the F336W filter. The UVIS2 intercept includes an offset of +0.5% due to changes in the EE at 10 pixels.

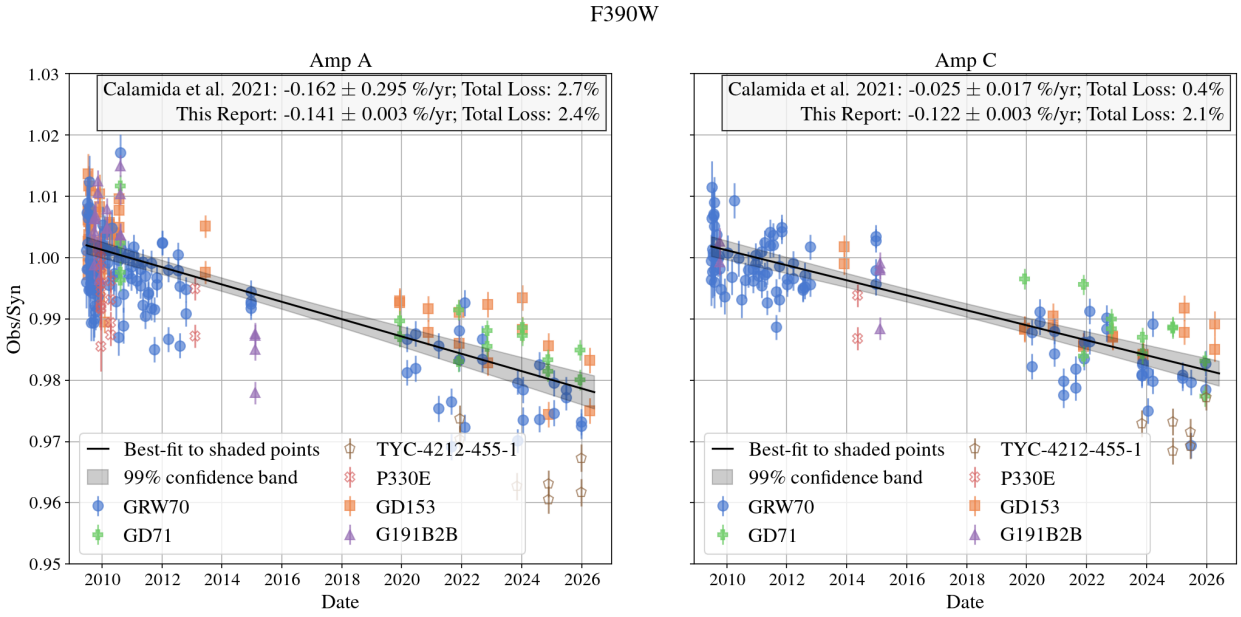

Figure 10: The same as Figure 1, but for the F390W filter.

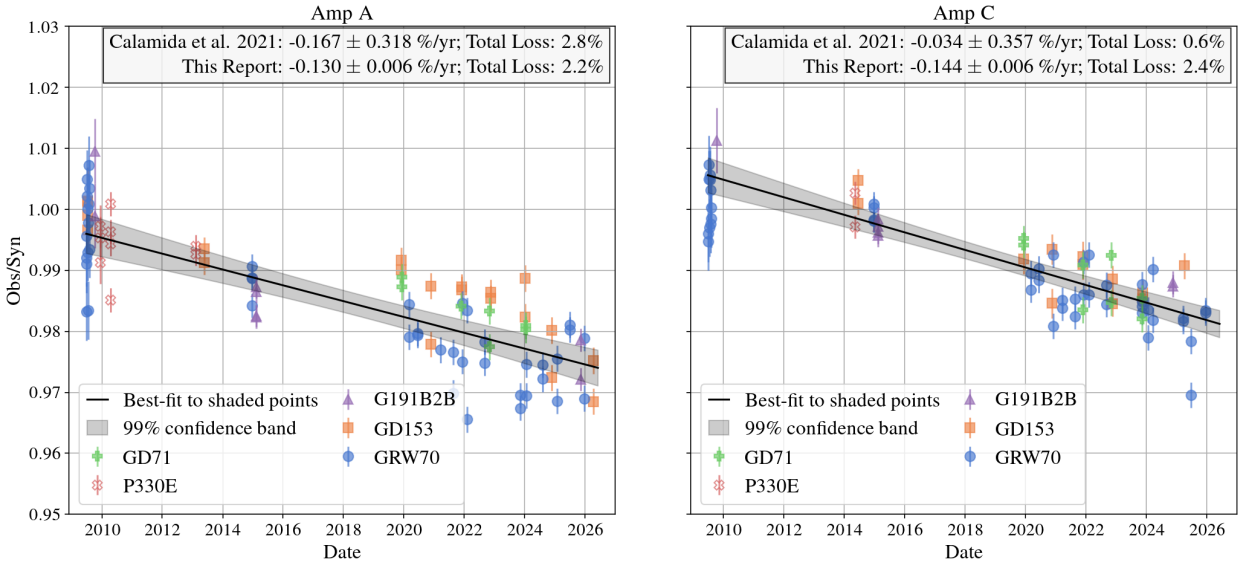

Figure 11: The same as Figure 1, but for the F410M filter.

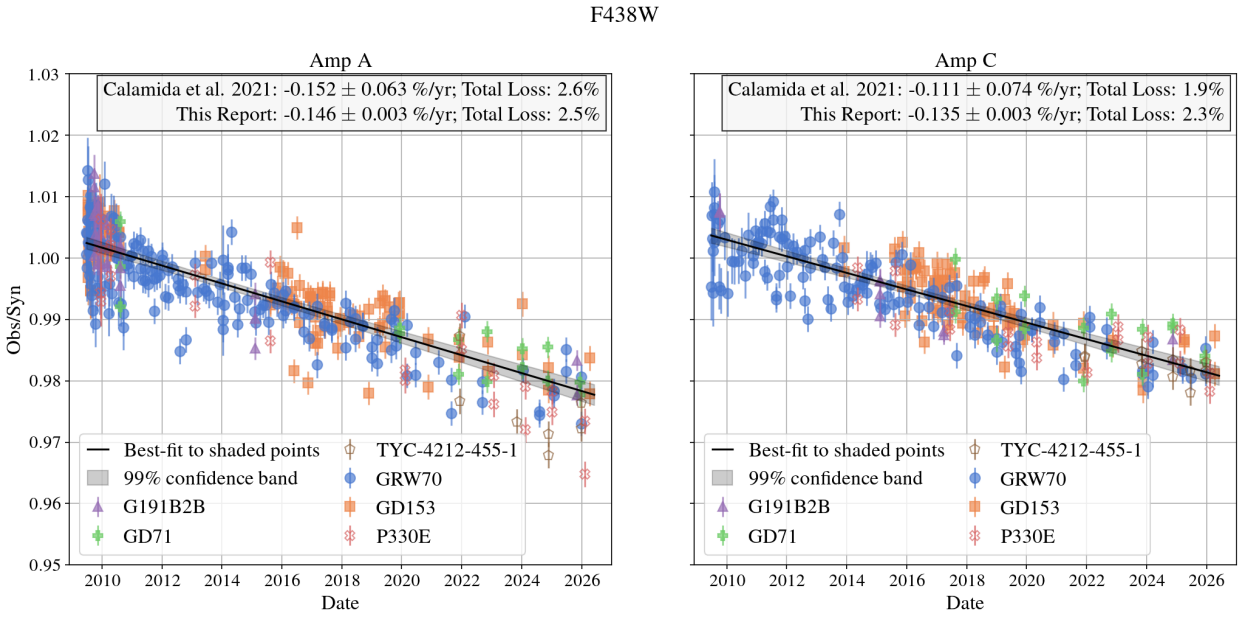

Figure 12: The same as Figure 1, but for the F438W filter.

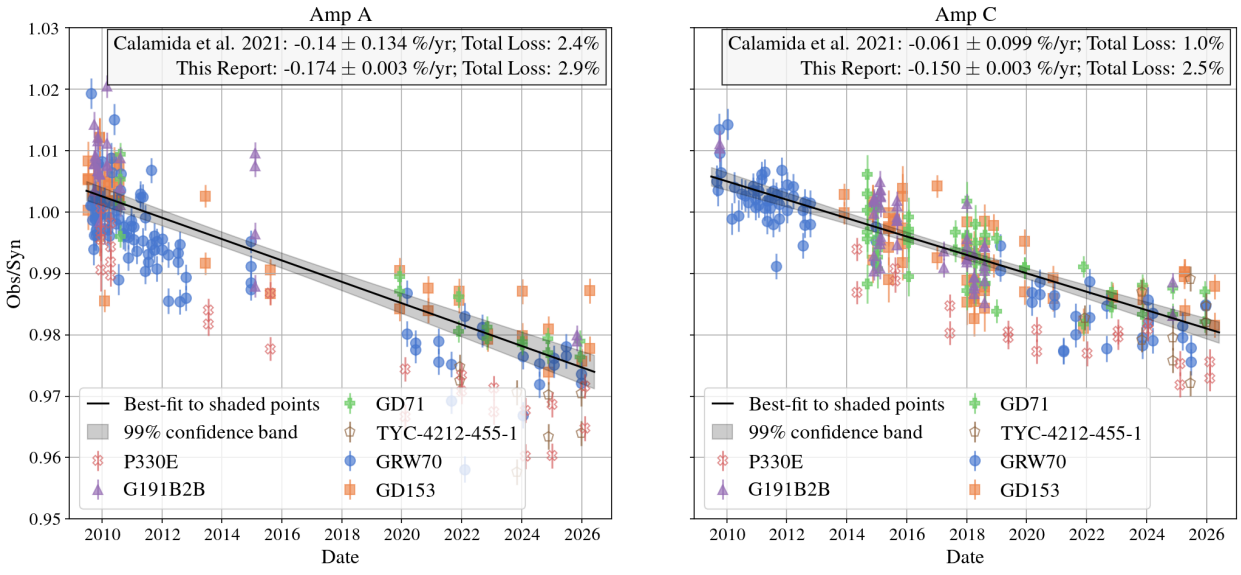

Figure 13: The same as Figure 1, but for the F475W filter.

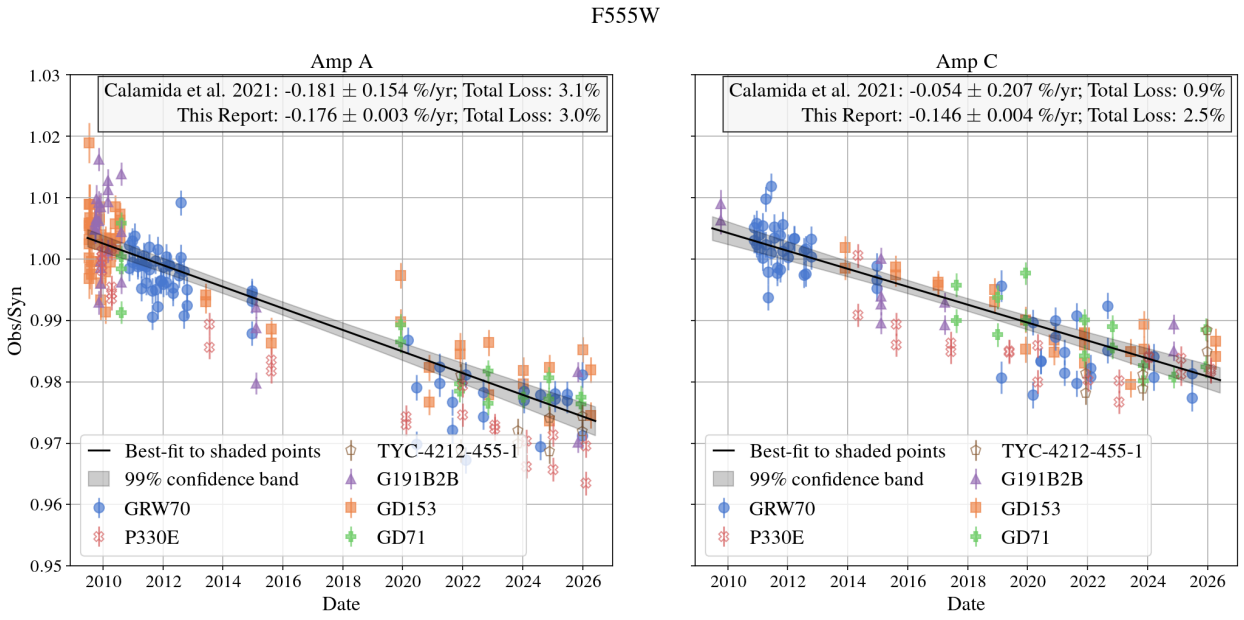

Figure 14: The same as Figure 1, but for the F555W filter.

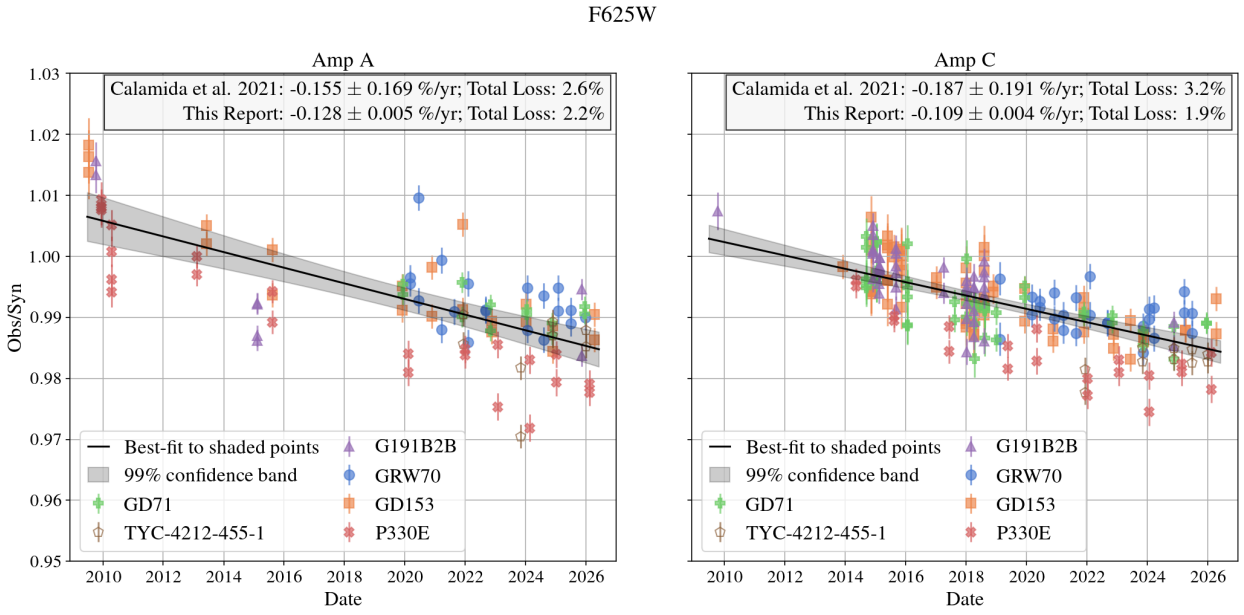

Figure 15: The same as Figure 1, but for the F625W filter. Limited UVIS2 observations were available prior to 2014.

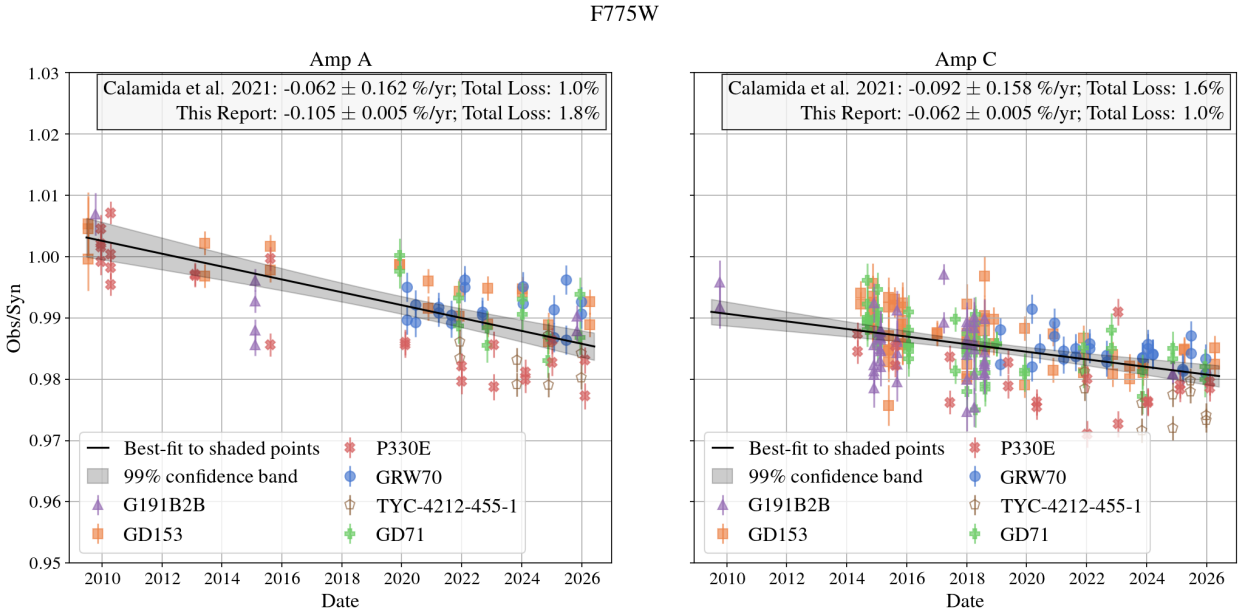

Figure 16: The same as Figure 1, but for the F775W filter. The UVIS2 intercept includes an offset of -0.5% due to updates in the EE(10) values. Limited UVIS2 observations were available prior to 2014.

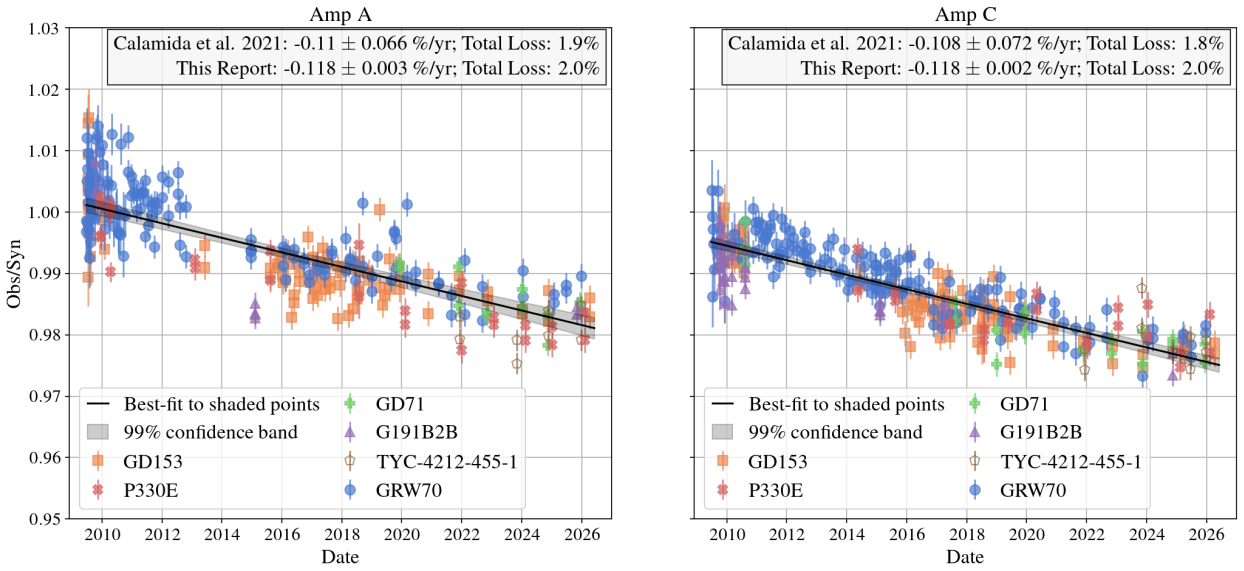

Figure 17: The same as Figure 1, but for the F814W filter. The UVIS2 intercept includes an offset of -0.5% due to updates in the EE(10) values.

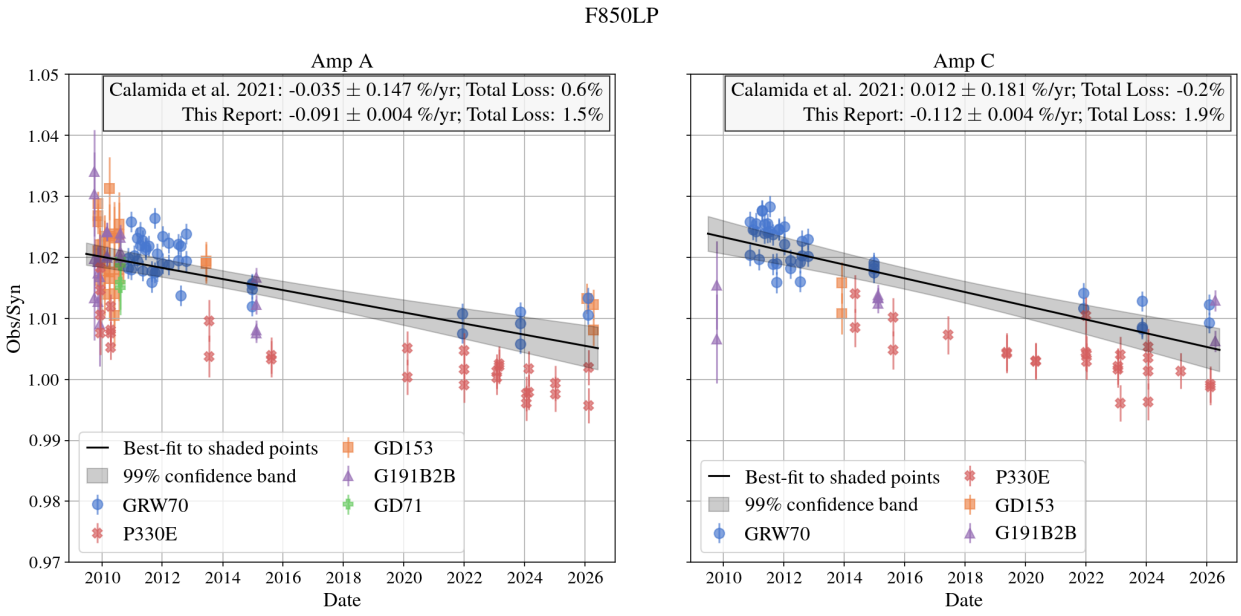

Figure 18: The same as Figure 1, but for the F850LP filter. The large offset in the intercept for both detectors $\sim +2\%$ is due to updates in the EE(10) values.

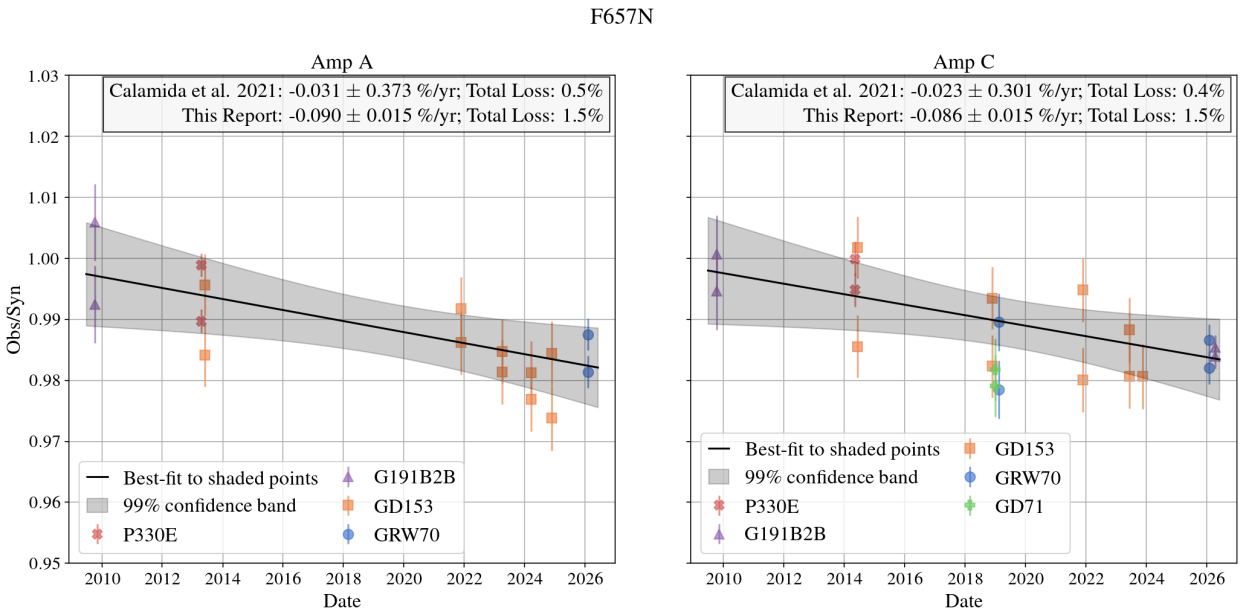

Figure 19: The same as Figure 1, but for the F657N filter.

Table 5: Slopes for individual stars on UVIS1. (For UV filters, slopes are for the second line segment after June 26, 2011).

Filter	GRW70 (% yr^{-1})	GD153 (% yr^{-1})	GD71 (% yr^{-1})	G191B2B (% yr^{-1})	P330E (% yr^{-1})
F218W	-0.248 ± 0.005	-0.220 ± 0.008	-0.50 ± 0.03	-	-
F225W	-0.208 ± 0.005	-0.180 ± 0.008	-0.20 ± 0.02	-	-0.14 ± 0.06
F275W	-0.173 ± 0.005	-0.182 ± 0.009	-0.07 ± 0.02	-	-0.19 ± 0.02
F336W	-0.087 ± 0.004	-0.065 ± 0.005	-0.084 ± 0.008	-0.083 ± 0.008	-0.109 ± 0.009
F390W	-0.146 ± 0.004	-0.128 ± 0.005	-0.125 ± 0.008	-	-
F438W	-0.148 ± 0.004	-0.155 ± 0.005	-0.122 ± 0.009	-0.151 ± 0.008	-0.174 ± 0.007
F475W	-0.181 ± 0.004	-0.158 ± 0.005	-0.175 ± 0.008	-0.180 ± 0.007	-0.185 ± 0.007
F555W	-0.180 ± 0.005	-0.157 ± 0.005	-0.150 ± 0.008	-0.201 ± 0.008	-0.194 ± 0.006
F606W	-0.172 ± 0.004	-0.133 ± 0.005	-0.19 ± 0.03	-0.15 ± 0.01	-0.175 ± 0.006
F625W	-	-0.13 ± 0.01	-0.08 ± 0.02	-	-0.162 ± 0.008
F775W	-	-0.08 ± 0.01	-0.15 ± 0.04	-	-0.136 ± 0.007
F814W	-0.123 ± 0.004	-0.091 ± 0.006	-0.13 ± 0.02	-	-0.120 ± 0.006
F390M	-0.144 ± 0.005	-	-	-	-
F410M	-0.147 ± 0.008	-0.13 ± 0.01	-	-	-
F467M	-0.171 ± 0.005	-0.129 ± 0.009	-	-	-
F547M	-0.171 ± 0.004	-0.124 ± 0.008	-	-	-0.188 ± 0.008
F621M	-	-0.099 ± 0.009	-0.10 ± 0.03	-	-0.162 ± 0.008
F689M	-	-	-	-	-0.132 ± 0.008
F763M	-	-0.09 ± 0.01	-	-	-
F845M	-	-0.06 ± 0.01	-	-	-0.09 ± 0.01
F280N	-	-0.13 ± 0.04	-	-	-
F343N	-	-0.09 ± 0.01	-	-	-
F373N	-	-0.14 ± 0.02	-	-	-
F395N	-	-0.16 ± 0.01	-	-	-
F469N	-	-0.17 ± 0.02	-	-	-
F487N	-	-0.20 ± 0.03	-	-	-
F502N	-0.15 ± 0.01	-0.15 ± 0.02	-	-	-
F631N	-	-	-	-	-
F645N	-	-0.11 ± 0.02	-	-	-
F656N	-	-0.08 ± 0.03	-	-	-
F657N	-	-0.09 ± 0.04	-	-	-
F658N	-	-	-	-	-
F665N	-	-0.13 ± 0.02	-	-	-
F673N	-	-0.14 ± 0.02	-	-	-
F680N	-	-	-	-	-
F953N	-	-0.04 ± 0.06	-	-	-0.12 ± 0.04
F200LP	-	-0.26 ± 0.01	-	-	-0.139 ± 0.007
F300X	-	-0.07 ± 0.02	-	-	-
F475X	-	-	-	-	-0.166 ± 0.007
F350LP	-	-0.125 ± 0.007	-0.159 ± 0.008	-	-0.111 ± 0.008
F600LP	-	-	-	-	-0.085 ± 0.008
F850LP	-0.086 ± 0.005	-0.07 ± 0.01	-	-	-0.068 ± 0.008

Table 6: Slopes for individual stars on UVIS2

Filter	GRW70 (% yr^{-1})	GD153 (% yr^{-1})	GD71 (% yr^{-1})	G191B2B (% yr^{-1})	P330E (% yr^{-1})
F218W	-0.258 ± 0.003	-0.201 ± 0.006	-0.24 ± 0.01	-0.223 ± 0.009	-
F225W	-0.227 ± 0.003	-0.181 ± 0.007	-0.10 ± 0.01	-0.173 ± 0.008	0.22 ± 0.05
F275W	-0.194 ± 0.004	-0.165 ± 0.008	-0.107 ± 0.009	-0.118 ± 0.008	-0.14 ± 0.02
F336W	-0.112 ± 0.004	-0.125 ± 0.008	-0.092 ± 0.009	-0.12 ± 0.01	-0.12 ± 0.01
F390W	-0.134 ± 0.004	-0.11 ± 0.01	-0.22 ± 0.03	-	-
F438W	-0.147 ± 0.004	-0.158 ± 0.008	-0.11 ± 0.02	-0.12 ± 0.01	-0.11 ± 0.01
F475W	-0.167 ± 0.004	-0.126 ± 0.009	-0.12 ± 0.01	-0.180 ± 0.009	-0.12 ± 0.01
F555W	-0.171 ± 0.006	-0.15 ± 0.01	-0.13 ± 0.02	-0.11 ± 0.01	-0.09 ± 0.01
F606W	-0.165 ± 0.004	-0.136 ± 0.005	-0.145 ± 0.008	-0.183 ± 0.007	-0.10 ± 0.01
F625W	-0.04 ± 0.02	-0.114 ± 0.009	-0.086 ± 0.009	-0.13 ± 0.01	-0.12 ± 0.01
F775W	-0.04 ± 0.02	-0.079 ± 0.009	-0.08 ± 0.01	-0.05 ± 0.01	-0.06 ± 0.01
F814W	-0.127 ± 0.004	-0.127 ± 0.005	-0.117 ± 0.007	-0.111 ± 0.008	-0.08 ± 0.01
F390M	-0.153 ± 0.005	-	-	-	-
F410M	-0.145 ± 0.008	-0.16 ± 0.02	-	-	-
F467M	-0.185 ± 0.005	-	-	-	-
F547M	-0.159 ± 0.006	-0.162 ± 0.007	-0.21 ± 0.01	-0.144 ± 0.006	-0.14 ± 0.02
F621M	-0.12 ± 0.02	-	-0.04 ± 0.02	-0.04 ± 0.01	-0.16 ± 0.02
F689M	-	-	-	-	-0.10 ± 0.02
F763M	-	-	-	-	-
F845M	-	-	-	-0.01 ± 0.01	-0.10 ± 0.01
F280N	-	-0.18 ± 0.04	-	-	-
F343N	-	-0.08 ± 0.02	-	-	-
F373N	-	-0.13 ± 0.05	-	-	-
F395N	-	-0.15 ± 0.02	-	-	-
F469N	-	-0.16 ± 0.02	-	-	-
F487N	-	-0.18 ± 0.06	-	-	-
F502N	-	-0.16 ± 0.02	-	-0.139 ± 0.009	-
F631N	-	-	-	-	-
F645N	-	-	-	-	-
F656N	-	-	-	-	-
F657N	-	-0.11 ± 0.05	-	-	-
F658N	-	-0.17 ± 0.04	-	-	-
F665N	-	-	-	-	-
F673N	-	-	-	-	-
F680N	-	-	-	-	-
F953N	-	-0.0 ± 0.1	-	-	0.05 ± 0.05
F200LP	-	-	-	-	-0.14 ± 0.01
F300X	-	-0.02 ± 0.02	-	-	-
F475X	-	-	-	-	-0.11 ± 0.01
F350LP	-	-0.25 ± 0.03	-0.14 ± 0.02	-	-0.12 ± 0.01
F600LP	-	-	-	-	-0.10 ± 0.01
F850LP	-0.097 ± 0.006	-	-	-	-0.09 ± 0.02